CFD modeling for moving jet penetrating cohesive soil

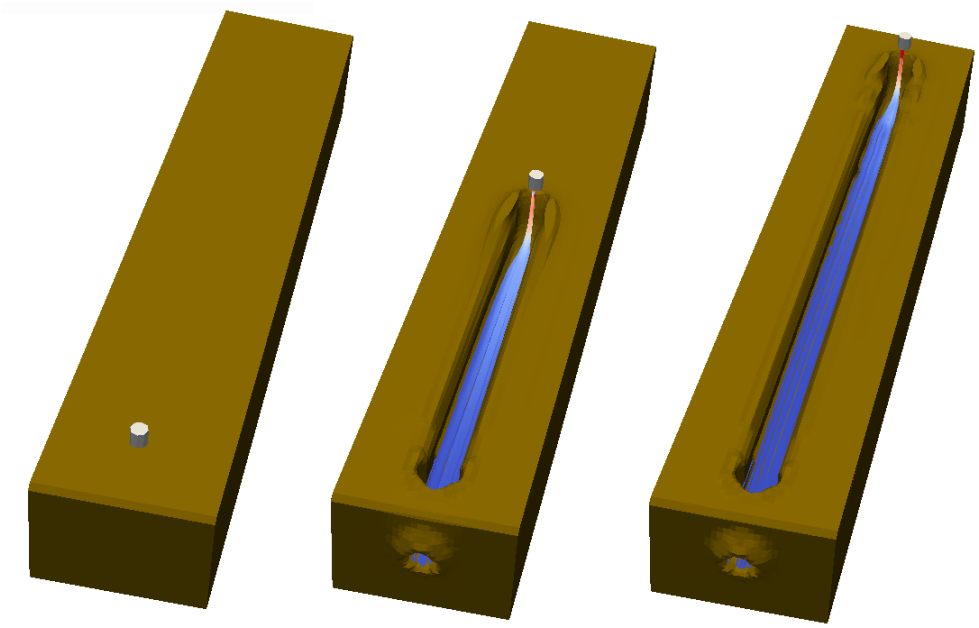

Boyao Wang

CFD modeling for moving jet penetrating cohesive soil

Master of Science Thesis

For the degree of Master of Science in Offshore and Dredging Engineering at Delft University of Technology

By

Boyao Wang
student number: 4735277

Thesis committee:	Dr.ir. G.H. Keetels	TU Delft
	Dr.ir. A. Jarquin Laguna	TU Delft
	Dr.ir. AH van Zuijlen	TU Delft

Faculty of Mechanical, Maritime and Materials Engineering (3mE) · Delft University of Technology

Contents

Summary **v**

List of Figures **vii**

List of Tables **xiii**

List of Symbols **xiv**

Abbreviations **xviii**

1 Introduction **1**

1.1 Background 1

1.1.1 Jetting process description 2

1.2 Research questions and objectives 4

1.3 Approach 5

1.4 Outline 6

2 Physics of moving jet penetrating cohesive soil **8**

2.1 Hydraulic loads on soil cavity walls during jetting 8

2.2 Failure modes during jetting 10

3 Modeling strategies **15**

3.1 Moving jet modeling 15

3.2 Soil modeling 17

3.3 Sediment transport modeling 19

3.3.1 Governing equations 21

3.4 Turbulence modeling 22

3.4.1 Averaging method 22

3.4.2 Buoyant $k - \epsilon$ model 23

4 Numerical techniques **27**

4.1 Discretization methods and numerical schemes 28

4.1.1 Discretization of Navier Stokes equations 28

4.1.2 Numerical schemes 31

4.2 Boundary conditions 32

4.3 Solution algorithms 33

4.4 Dynamic mesh algorithms 37

4.4.1 Basic equations for dynamic mesh 37

4.4.2 Topological change dynamic mesh 38

5 Numerical validation for dynamic mesh model 44

5.1 Lock-exchange physics 45

5.2 Initial and boundary conditions 46

5.3 Results 48

5.3.1 Flow patterns 48

5.3.2 Dimensionless front speed *Froude* number F_H 51

5.3.3 COG comparison and mass conservation check 54

5.4 Summary and remarks 55

6 CFD modeling of moving jet penetrating cohesive soil 57

6.1 Numerical setup 58

6.1.1 Mesh setup and mesh sensitivity check 58

6.1.2 Initial conditions setup 61

6.1.3 Boundary conditions setup 63

6.2 Comparison with experiment 65

6.2.1 Failure modes during jetting 66

6.2.2 Dimensionless soil cavity depth at different traverse velocity with a jet ratio 19.5 67

6.2.3 Clay surface dislodgement rate 68

7 Analysis based on CFD simulation 71

7.1 Soil volume dislodgement rate with respect to jet traverse velocity . 71

7.2 Pressure on soil surface over time 73

7.3 Shear plane change as a function of time 74

7.4 Jet inclination angle and deflection distance 76

8 Conclusions and recommendations **78**

8.1 Conclusions 78

8.1.1 Dynamic mesh model 79

8.1.2 Validation with experiment 79

8.1.3 Analysis based on CFD simulation 80

8.2 Summary and Recommendations 80

A Derivation of drift-flux model **82**

Bibliography **86**

Summary

In dredging operation, the high-pressure water jet is widely used for the excavation of soil. To study the jetting process and optimize the design of the dredging devices, moving vertical water jet penetrating cohesive soil experiments were carried out by Nobel (2013). However, in terms of the design optimization for dredging devices, it is not easy to change the jet scale and soil properties during the experiment due to time and economic constraints. Some detailed physics during the jetting process, e.g. pressure on the soil surface and shear plane inside the soil during jetting, were also not monitored by doing the experiment. Therefore, numerical simulation is chosen in this thesis to optimize the design of dredging devices and study the physics of the jetting process.

A CFD (computational fluid dynamics) numerical model is used in this thesis to simulate the moving jet penetrating cohesive soil. The soil is modeled as a Bingham plastic(Bingham, 1922). By using the Bingham plastic model, the soil can be modeled as a fluid with a stress strain rate behavior implementing into the CFD model. The sediment transport is modeled by using drift-flux model(Goeree et al., 2016). In drift-flux model, all sediment phases are considered as a mixture. By solving the continuity and the momentum equations for a mixture instead of each phase, the drift-flux model can save computational power. The moving jet modeling is achieved by using the dynamic mesh algorithms AMI (arbitrary mesh interface) and A/R (cell layer addition removal). By combining these two dynamic mesh algorithms, a steady mesh region can be created which reduce the numerical error introduced by dynamic mesh. Combining AMI and A/R also allows for multiple nozzles modeling, which is beneficial for the optimization of dredging devices. The CFD numerical model for simulating moving jet penetrating

cohesive soil has been validated with the experiment of Nobel. The failure modes during jetting, dimensionless soil cavity depth and clay surface dislodgement rate are compared with the previous experiment. After the validation, an analysis of the jetting process based on this CFD model is accomplished proving the CFD model can reveal the details of the soil failure process during jetting.

Two of the failure modes existing in the previous experiment, which are penetrating jet and deflecting jet, are successfully predicted by the numerical model. The soil dimensionless cavity depth calculated by using CFD model also shows a similar trend and magnitude as the previous experiment. A comparison of soil surface dislodgement rate between experiment and CFD model is done. The soil surface dislodgement rate of the experiment is in between the maximum and minimum transient soil surface dislodgement calculated by the CFD model.

After the validation of the CFD model, the pressure on the soil surface as a function of time, the shear plane change over time, the soil volume dislodgement rate with respect to jet traverse velocity, the jet inclination angle and the deflection distance are analyzed. From the analysis, the following conclusions are drawn. To remove the cohesive soil, the pressure is building up on the soil surface until the pressure exceeds the shear strength of the soil. In order to clarify the shear plane of the soil during jetting, the shear rate is calculated and used to define the shear plane in this thesis. The shear plane of the deflecting jet does not change over time while the shear plane of the penetrating jet shows a periodic behavior. Similarly, the deflection distance of the deflecting jet keeps a constant value over time while that of penetrating jet shows a periodic behavior. Notably, for a penetrating jet, the period of shear plane change is the same as the period of deflection distance. It is also found that for a single moving jet, the soil volume dislodgement rate increases as the jet traverse velocity increases when jet traverse velocity v_t is lower than $1.83 m/s$.

List of Figures

1.1 under water operation of TSHD(Groen, 2016) 2

1.2 Bottom view of a draghead with nozzles(Groen, 2016) 2

1.3 Moving jet penetrating cohesive material from experiment(Nobel, 2013). 3

1.4 Failure mechanism of cohesive soil during jetting(Nobel, 2013). Where τ_b is the shear stress, P_{stag} is the jet stagnation pressure, F_r is the resistance force of the soil, su is the shear strength of the soil, A_s is the area of the shear surface. 4

2.1 Loading conditions of a moving vertical jet penetrating a cohesive soil bed. 9

2.2 Penetrating jet: regular pattern of soil that is pushed up at the soil cavity edge (a) overview, (b) soil cavity traversal cross-sections. Test conditions: $p_j/su = 21$, $D_n = 32.5$ mm, $v_t = 0.25$ m/s. (Nobel, 2013) 10

2.3 Deflecting jet: vertically oriented nerves in non-deflection zone. Test conditions: (a) $p_j/su = 25.8$, $D_n = 20$ mm, $v_t = 0.15$ m/s, (b) $p_j/su = 8.9$, $D_n = 5$ mm, $v_t = 1$ m/s. (Nobel, 2013) 11

2.4 Dispersing jet: typical shallow soil cavity shape (a) top view, (b) transverse cross section. Test conditions: $p_j/su = 9$, $D_n = 32.5$ mm, $v_t = 1$ m/s. (Nobel, 2013) 12

2.5 Hydro fracturing: (a) top view, with two planes of weaknesses along which the jet had penetrated the soil surface, (b) longitudinal cross section. Test conditions: $D_n = 32.5$ mm, $p_j = 0.82\ MN/m^2$, $v_t = 0.125\ m/s$, $su = 70\ kN/m^2$. (Nobel, 2013) 12

2.6 Definition of nozzle traverse velocity v_t, soil horizontal propagation speed $u_{f,h}$, soil vertical propagation speed $u_{f,v}$ (Nobel, 2013) 13

2.7 Definition of jet zones of penetrating jet. Zone I is the non-deflection zone, zone II is the deflection zone. When the jet traverse velocity is larger, jet flow follows a inclination line 14

2.8 The definition of deflecting jet, which has only a deflection zone . . 14

3.1 Shear stress and shear rate relationship of Newtonian fluid and non-Newtonian fluid 18

3.2 Typical velocity profile for a turbulent boundary layer(Wilcox et al., 1998). $y^+ = yu_\tau/\nu$, $u^+ = u/u_\tau$. y is the distance from the wall to the center of the first grid-cell from the wall. u_τ is the wall friction velocity. ν is the kinetic viscosity of the fluid. u is the flow velocity. 26

4.1 2D unknowns arrangement in collocated grid on cell Ω_{ij}, $\rightarrow$ and $\uparrow$ mean the vector field e.g. velocity, $\bullet$ means the scalar field e.g. pressure, i, j represent the index of the cell 29

4.2 Stencil of collocated grid in 2D, $-$ and $|$ mean velocity, $\bullet$ means pressure 30

4.3 Definition of `local min` scheme. 31

4.4 Boundary condition set up for explanation, inflow condition is applied to the left, outflow condition is applied to the right, no-slip condition is applied on the bottom, free surface condition is applied on the top. The domain has a width of $w = a$ and length of $L = b$. 32

4.5 Flow chart of SIMPLE algorithm(Holzinger, 2015) 34

4.6 Flow chart of PISO algorithm(Holzinger, 2015) 36

4.7 Flow chart of PIMPLE algorithm(Holzinger, 2015) 37

4.8 AMI interpolation between interface(Mangani et al., 2014), where NB means the neighbour point, C is cell under consideration 40

4.9 Stitching and splitting of mesh in sliding mesh algorithm(Piscaglia et al., 2014) 40

4.10 Layer addition/removal dynamic mesh algorithm - layer addition . . 41

4.11 Layer addition/removal dynamic mesh algorithm - layer removal . . 42

4.12 2D sphere drop with both AMI and A/R dynamic mesh algorithm . 43

5.1 Experiment set up for lock-exchange test. The denser fluid is put to the left of the lock gate with $\rho_2 = 1000kg/m^3$ and the lighter fluid is put to the right of the lock gate with $\rho_1 = 996kg/m^3$. The lock gate is put in the middle of them. All fluids are sealed inside the surrounding wall. 46

5.2 Boundary condition for lock-exchange test. No slip wall boundary condition for velocity field and zero gradient for pressure field . . . 47

5.3 The above mesh set up is for only using A/R case. The below mesh set up is for AMI combined A/R case. Time = 0 sec, mesh moving velocity = 0.01m/s. 47

5.4 The above mesh set up is for only using A/R case. The below mesh set up is for AMI combined A/R case. Time = 25 sec, mesh moving velocity = 0.01m/s. 48

5.5 Flow pattern calculated by A/R dynamic mesh algorithm at 21 seconds. Mesh moving velocity: 0.01 m/s, 0.02 m/s, 0.04 m/s and 0.06 m/s 49

5.6 Flow pattern calculated by AMI + A/R dynamic mesh algorithm at 21 seconds. Mesh moving velocity: 0.01 m/s, 0.02 m/s, 0.04 m/s and 0.06 m/s 50

5.7 Dimensionless front position of density flow over time of numerical lock-exchange experiment 51

6.1 Mesh region layout of moving jet penetrating cohesive soil clay using AMI and A/R at $t = 0s$, mesh moving velocity $v_{mesh} = 1.5m/s$ . . . 59

6.2 Mesh region layout of moving jet penetrating cohesive soil clay using AMI and A/R at $t = 1s$, mesh moving velocity $v_{mesh} = 1.5m/s$ . . . 59

6.3 Mesh sensitivity check: dimensionless soil cavity depth comparison at different jet traverse velocity of two mesh sizes ($0.01m$ and $0.005m$). 61

6.4 α_s layout in whole computational domain in 3D 62

6.5 Side view of initial concentration field : the clay has a 1.5 m length, 0.15 m width(not shown in this figure), 0.28 m depth. The blue part is water, the red part is clay. The length, width and height of the computational domain are $1.8m$, $0.15m$ and $0.3m$. 62

6.6 The soil volume concentration profile along the red dash line in the left figure is assumed to follow the volume concentration changing rule of figure(a). In figure(a), the volume concentration of soil at the soil water interface increases gradually, while that in figure(b) changes sharply. 64

6.7 Boundary conditions setup side view 64

6.8 Boundary conditions setup front view 64

6.9 Residual convergence check of the case when jet ratio is $p_j/su = 19.5$ and jet traverse velocity $v_t = 1.83m/s$. Residual convergence of soil volume concentration α_s, pressure P_{rgh} and velocity in three directions U_x, U_y and U_z are checked. The residual tolerance of α_s, P_{rgh} and U are 10^{-16}, 10^{-10} and 10^{-9} respectively. 65

6.10 Failure modes calculated from CFD. Figure (a) represents the penetrating jet, with jet inlet velocity $V_{in} = 45m/s$, jet ratio $p_j/su = 38$ and jet traverse velocity $V_t = 0.5m/s$. Figure (b) represents the deflecting jet with jet inlet velocity $V_{in} = 30m/s$, jet ratio $p_j/su = 19.5$ and jet traverse velocity $V_t = 1.83m/s$. The brown parts represent soils, while the red parts represents jet flow. 66

6.11 Dimensionless soil cavity depth at different jet traverse velocity when jet ratio $p_j/su = 19.5$. The uncertainty of experimental work is 20%, see red uncertainty bar. The dots represent the results calculated by laminar solver. The triangles represent the results calculated by $buoyant - k - \epsilon$ RANS model. The cross symbols represent experimental result from Nobel (2013). The dash lines are the linear trend lines of results calculated using laminar and RANS solver. The solid line is the linear trend line of experimental results(Nobel, 2013). 67

6.12 The amount of clay removed after $0.003s$ jetting from experiment(Nobel, 2013). From the figure, around 6 cells are removed after jetting. The jet traverse velocity is $v_t = 0.5\ m/s$ and jet ratio is $p_j/su = 38$. . . . 69

6.13 The soil surface dislodgement rate as a function of time calculated by CFD model. The green dash line represents the soil surface dislodgement rate of experiment, which is equal to 0.078 mm^2/s. . . 70

7.1 The soil concentration contour change as a function of time. The jet ratio is $p_j/su = 19.5$ and the jet traverse velocity is $v_t = 1.83m/s$. 72

7.2 Soil dislodgement rate with respect to jet traverse velocity v_t. The jet ratio is $p_j/su = 19.5$. 72

7.3 Pressure profile on soil surface of deflecting jet over time 73

7.4 Shear plane patterns over time of deflecting jet. Jet traverse velocity is $v_t = 1.83\ m/s$. Jet ratio is $p_j/su = 19.5$. The shear rate is plotted on the soil. The shear plane pattern is marked by the white curve. . 75

7.5 Shear plane patterns over time of penetrating jet. Jet traverse velocity is $v_t = 0.5\ m/s$. Jet ratio is $p_j/su = 38$. The strain rate is plotted on the soil. The shear plane is marked by the white curve. Two periods of shear plane change are shown. The period of the shear plane change is 0.02 s. 75

7.6 Definition of jet inclination angle and deflecting distance. U_x and U_z are the x and z components of jet center line velocity U. The deflecting distance is defined as the vertical distance between the soil surface and deflecting point. The deflecting point is the position where jet inclination angle is equal to 5 degree. 76

7.7 The deflection distance over time of penetrating jet and deflecting jet. The deflection distance is defined as the vertical distance between the soil surface and deflecting point. The deflecting point is the position where jet inclination angle is equal to 5 degree. The penetrating jet has a traverse velocity of 0.5 m/s and jet ratio 38. The deflecting jet has a traverse velocity of 1.83 m/s and jet ratio 19.5. 77

List of Tables

3.1 Overview of CFD studies with RANS on PTIJ 16

5.1 Heavy density current F_H error comparison among different mesh moving speed 52

5.2 Light density current F_H error comparison among different mesh moving speed 53

5.3 Mass conservation check at 21 seconds 54

5.4 COG position check at 21 seconds 55

6.1 Mesh sensitivity check: dimensionless soil cavity depth at different jet traverse velocity of two mesh sizes($0.01m$ and $0.005m$) 60

6.2 Boundary conditions set up at different positions for all variables . . 63

List of Symbols

Greek symbols

α_k	Volume concentration of phase k	$-$
$\dot{\gamma}$	Shear rate	$1/s$
ϵ	Turbulent dissipation rate	m^2/s^3
μ	Dynamic viscosity	Ns/m^2
ν_t	Turbulence eddy viscosity	m^2/s
ρ_k	Density of phase k	kg/m^3
ρ_m	Density of mixture	kg/m^3
τ	Shear stress	N/m^2
τ_y	Yield stress	N/m^2
θ_j	Jet inclination angle	deg

Roman symbols

$\mathbf{g}$	Gravitational acceleration vector	m/s^2
$\mathbf{T_k^t}$	Turbulent shear stress	N/m^2
$\mathbf{T_k}$	Viscous shear stress	N/m^2
$\mathbf{u_s}$	Velocity of the boundary surface of moving mesh	m/s

$\mathbf{u_{km}}$	Relative velocity between mixture velocity and phase k	m/s
$\mathbf{u_{kr}}$	Relative velocity between the carrier fluid and phase k	m/s
$\mathbf{u_k}$	Velocity of phase k	m/s
$\mathbf{u_m}$	Mixture velocity	m/s
C_f	Skin friction coefficient	$-$
c_k	Mass fraction of phase k	$-$
C_μ	Turbulence model constant	$-$
D_n	Nozzle diameter	m
F_H	Froude number of lock-exchange test	$-$
G_k	Buoyancy production/destruction of turbulence kinetic energy	m^2/s^3
k	Turbulent kinetic energy	m^2/s^2
l	Turbulence length scale	m
Nu	Kinetic viscosity	m^2/s
p	Pressure	N/m^2
p_j	Jet pressure	N/m^2
P_k	Production of turbulence kinetic energy	m^2/s^3
su	Shear strength of the soil	N/m^2
U	Front speed of the density current in lock-exchange test	$-$
$u_{f,h}$	Soil horizontal propagation velocity	m/s
$u_{f,v}$	Soil vertical propagation velocity	m/s
V_0	Total volume	m^3
V_k	Volume of phase k	m^3

v_t	Jet traverse velocity	m/s
Zc	cavity depth of the soil	m

Abbreviations

2D Two Dimensional

3D Three Dimensional

A/R cell layer addition/removal

AMI arbitrary mesh interface

CFD computational fluid dynamics

COG center of gravity

CPU central processing unit

CV control volumes

DNS direct numerical simulation

FDM finite difference method

FEM finite element method

FVM finite volume method

GGI general grid interface

GPU graphics processing unit

HRKE high Reynolds number $k - \epsilon$ model

LES Large Eddy Simulation

LHS left hand side

LRKE low Reynolds number $k - \epsilon$ model

OpenFOAM Open-source Field Operation And Manipulation

PISO Pressure-Implicit with Splitting of Operators

PTIJ plane turbulent impinging jet

RANS Reynolds-averaged Navier Stokes

RHS right hand side

RNG Re-Normalization Group $k - \epsilon$ model

RSM Reynolds stress equation model

SCL space conservation law

SIMPLE Semi-Implicit Method for Pressure Linked Equations

SKO standard $k - \epsilon$ model

SKO standard $k - \omega$ model

SOD stand off distance

SST SST $k - \omega$ model

TSHD Tailing Suction Hopper Dredgers

Chapter 1

Introduction

1.1 Background

Dredging is an operation removing materials underwater from one location and relocating the materials to another. The purpose of dredging is mainly about land reclamation, maintenance of water ways and mining of construction materials. Dredging operations have to be done by using a dredger. There are two main types of dredgers, which are the mechanical dredger and the hydraulic dredger. The soil can be excavated using a mechanical dredger by cutting and a hydraulic dredger by jetting. Water jets are widely used in hydraulic dredging. A jet with high pressure and high flow velocity can penetrate the soils and brings them to suspension. For example, the dragheads of a TSHD (Tailing Suction Hopper Dredgers) are equipped with a water jet system, see Fig.1.2. During the dredging process, the water jets will fluidize and remove the soil to create a new depth of water. The under water operation of a TSHD is shown in Fig.1.1. This operation can be regarded as a moving jets penetrating soil process.

Figure 1.1: under water operation of TSHD(Groen, 2016)

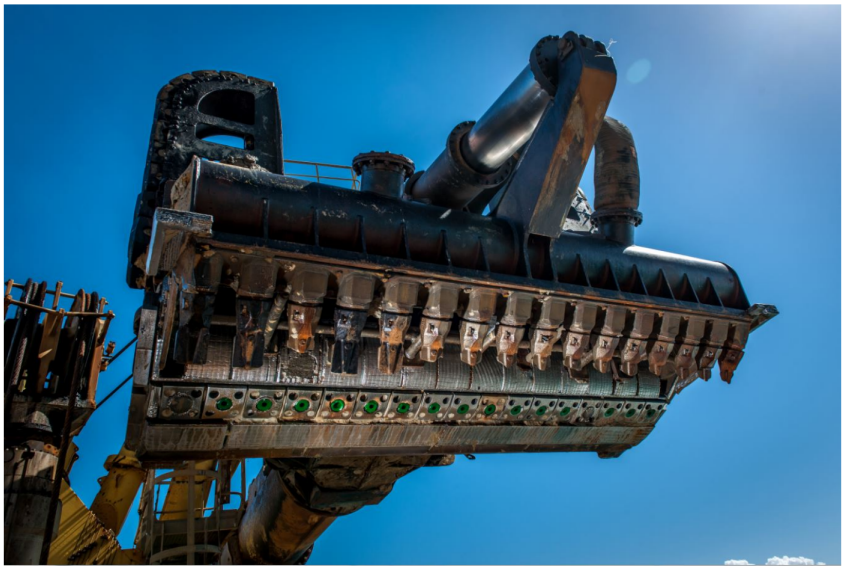

Figure 1.2: Bottom view of a draghead with nozzles(Groen, 2016)

1.1.1 Jetting process description

For sandy soils, the moving jet soil excavation operation works very well. However, for cohesive soil the moving jets cannot easily achieve a large production of soil. Therefore, questions about the process of a moving jet penetrating cohesive soil are frequently asked. Cohesive soil is defined as sticky soil which is usually composed of a mixture of clay, silt and sand. In cohesive soil, the clay particles are mainly

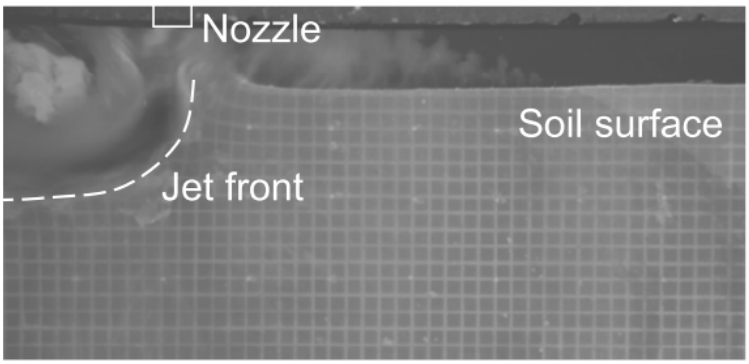

Figure 1.3: Moving jet penetrating cohesive material from experiment(Nobel, 2013).

responsible for the cohesive behavior. The pores in between the particles are fully or partially filled with water. The main characteristics of cohesive soils are: very low water permeability, high skeleton compressibility and plasticity.

Fig.1.3 shows the experimental result of moving jet penetrating cohesive soil(Nobel, 2013). Due to the traverse velocity of the nozzle and resistance of the soil, the jet flow in front of the soil is deflected as shown in Fig.1.3. It can be seen that the soil can be fluidized and removed by using the moving jet.

The main failure mechanism of soil during the jetting process can be classified by different forces exerting on the soil. The main forces exerting on the soil are(Nobel, 2013):

- The stagnation pressure on the soil: This force is exerting on the soil surface following the main direction of the jet flow. This force is caused by the mass flow of the jet.
- The shear force: The shear force is parallel to the flow direction, caused by the flow velocity and viscosity of water.

In cohesive soil, depending on the loading conditions, different shear surfaces are formed inside the soil. During jetting process, when the jet load exceeds the

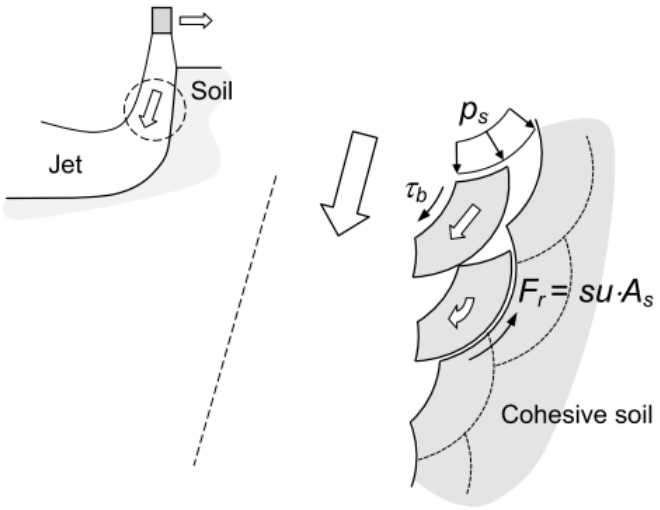

Figure 1.4: Failure mechanism of cohesive soil during jetting(Nobel, 2013). Where τ_b is the shear stress, P_{stag} is the jet stagnation pressure, F_r is the resistance force of the soil, su is the shear strength of the soil, A_s is the area of the shear surface.

strength of the soil, the soil will fail along these shear surfaces. This process can be found in Fig.1.4.

1.2 Research questions and objectives

To optimize the design of dredging devices and study the physics of the jetting process, moving jet penetrating cohesive soil experiment is carried out by Nobel (2013). However, in terms of optimization for dredging devices design, it is not easy to change the jet scale and soil properties during the experiment due to time and economic constraints. Besides, some detailed physics during the jetting process, e.g. pressure on the soil surface and shear plane inside the soil during jetting, cannot be monitored by doing the experiment.

Instead of experimental method, numerical modeling is also an alternative. By using numerical modeling method, the soil properties and jet scales are relatively

easier to change compared with the experiment, which means the optimization for dredging devices can be easily conducted. Besides, the detailed physics can also be monitored during the simulation. However, numerical simulation has never been carried out before and after the experimental work of Nobel. Therefore, the main objectives of this master thesis are:

- To evaluate a proper numerical approach, especially CFD (computational fluid dynamics) model, to study moving jet penetrating cohesive soil process.
- To validate the numerical model with the previous experimental work of Nobel by comparing the soil failure modes, soil cavity depth after jetting and soil surface dislodgement rate.
- To carry out analysis which was not recorded by the previous experiment based on this numerical model. The results which are not available in the experiment are the pressure profile on a fixed point of soil surface over time, the shear plane and the soil volume dislodgement rate over time.

1.3 Approach

The numerical approach used in this thesis is called computational fluid dynamics (CFD). The reason of using CFD is the cohesive soil clay, which is composed of both water and soil particles, can be modeled as a fluid mixture. In this thesis, the drift-flux model is used to calculate the sediment transport. The drift-flux model(Goeree et al., 2016), which is a simplification of Euler/Euler model, considers all phases as a mixture. Instead of solving the momentum equations of each phase, drift-flux model solves only one mixture momentum equation, which saves computational power. To model the cohesive soil as a fluid, non-Newtonian fluid model Bingham plastic is used in this thesis. Bingham plastic model(Bingham, 1922) describes the fluid with a stress strain rate behavior, which is convenient for implementing the soil into the CFD model.

The partial differential equations in drift-flux model are solved using finite volume method (FVM). The software OpenFOAM (Open-source Field Operation And Ma-

nipulation)(Greenshields, 2018) is used in this thesis for simulation. OpenFOAM is an open source software programmed by C++, which can be modified by user. Drift-flux model is also available in OpenFOAM, which is called *driftFluxFoam*.

To model the moving jet, dynamic mesh algorithms AMI (arbitrary mesh interface) and A/R (cell layer addition/removal) are used in this master thesis. Unfortunately, dynamic mesh algorithm is not available in *driftFluxFoam*. To solve this problem, a drift-flux solver with dynamic mesh algorithm, which name is `driftFluxDyMFoamv1812`, is created by author of this thesis.

1.4 Outline

In Chapter 2, the physics of moving jet penetrating cohesive soil is explained. Five loading conditions and four types of failure modes during jetting will be introduced.

In Chapter 3, the modeling strategies used in this thesis will be explained. The moving jet is modeled by using dynamic mesh algorithms AMI (arbitrary mesh interface) and A/R (cell layer addition removal). The drift-flux model is used for describing the sediment transport. Bingham plastic model, which can describe cohesive soil by a stress strain rate behavior, is used modeling the cohesive soil. $Buoyant - k - \epsilon$ model, which includes the modulation of turbulent kinetic energy caused by density stratification effects, is applied to model the turbulence of the flow.

In Chapter 4, numerical techniques used in this thesis will be introduced. The derivation of discretization for Navier-Stokes equations in collocated mesh grid using finite volume method (FVM) is done in section 4.1. The numerical schemes used in this thesis are also introduced in section 4.1. The implementation of boundary conditions is introduced in section 4.2. Solution algorithms: SIMPLE, PISO and PIMPLE are explained and derived in section 4.3. Dynamic mesh algorithms AMI and A/R are explained in section 4.4.

In chapter 5, a numerical validation for dynamic mesh models used in this thesis is conducted by doing a lock-exchange numerical experiment. The results show that

a combination of AMI and A/R has lower numerical error than only using A/R dynamic mesh algorithm.

In Chapter 6, moving jet penetrating cohesive soil CFD modeling is accomplished. In this chapter, the numerical setup including mesh, boundary conditions and initial conditions are introduced. Mesh and residual convergence are also checked before comparing the results with the experiment. After convergence check, validation of CFD model with previous experiment is conducted in section 6.2.

Analysis based on CFD, which was not recorded by the experiment are shown in chapter 7. Soil volume dislodgement rate w.r.t jet traverse velocity, pressure on soil surface over time, shear plane change over time, jet inclination angle and jet deflecting distance are investigated.

Finally, the conclusions of this thesis and recommendations for future work are given in chapter 8.

Chapter 2

Physics of moving jet penetrating cohesive soil

In this chapter, the physics of moving jet penetrating cohesive soil will be introduced. There are several failure modes of soil during jetting when the nozzle has different traverse velocities and jet ratio(Nobel, 2013). In the following sections, different failure modes of the soil and the soil failure mechanism during jetting will be described.

2.1 Hydraulic loads on soil cavity walls during jetting

The loading conditions of moving jet penetrating cohesive soil(Nobel, 2013) is shown in Fig.2.1.

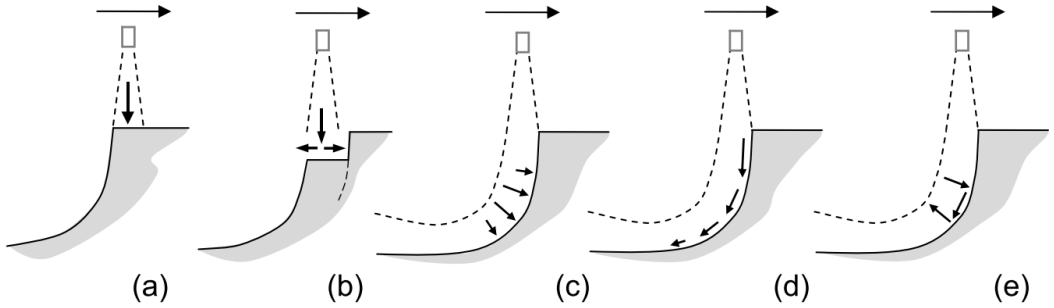

Figure 2.1: Loading conditions of a moving vertical jet penetrating a cohesive soil bed.

There are five loading conditions (a) - (e) shown in Fig.2.1:

- condition (a): Jet pressure is normally exerting on the soil surface. Jet pressure is equal to the jet stagnation pressure p_{stag}.
- condition (b): Besides the normal stagnation pressure parallel to the jet flow direction exerting on the soil, normal pressure perpendicular to the jet flow direction is also exerting on the soil.
- condition (c): Due to the deflection of the jet flow, the pressure exerting on the soil is normal to the soil surface.
- condition (d): Shear stress parallel to the soil is exerting on the soil surface.
- condition (e): Due to turbulence pressure fluctuations, temporary normal pressure is exerting on the soil.

As the SOD(stand off distance: the distance between the jet outlet and soil surface) of the jet is about one time the nozzle diameter(30 mm), the cavitation of the jet can be neglected in the study.

2.2 Failure modes during jetting

Moving vertical jet penetrating cohesive material experiment has been done by Nobel (2013) with different jet traverse velocity v_t and jet ratio p_j/su, where p_j is the jet pressure, su is the shear strength of the soil. In his work, four different types of failure modes are found:

- Penetrating jet: (1) Penetrating jet happens when jet ratio $p_j/su > 12$ and the jet traverse velocity $v_t \leq u_{f,h}$. $u_{f,h}$ is the soil horizontal propagation velocity, which is defined in Fig.2.6. (2) The soil cavity is narrow and deep, with a cavity width of 1 to 1.5 times the jet diameter. (3) A soil wall with vertical and curving nerves is built. The vertical nerves are present in non-deflection zone while the curving nerves are in deflection zone. (4) The dislodged soil is completely fluidized.

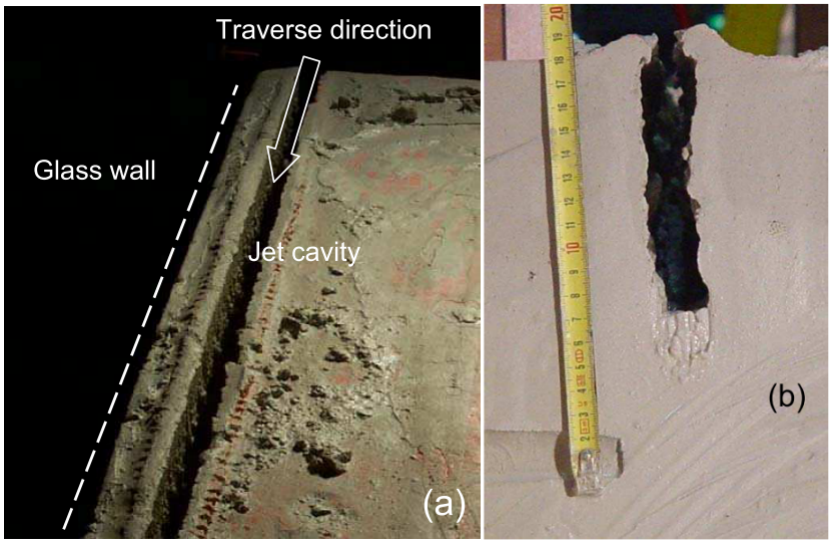

Figure 2.2: Penetrating jet: regular pattern of soil that is pushed up at the soil cavity edge (a) overview, (b) soil cavity traversal cross-sections. Test conditions: $p_j/su = 21$, $D_n = 32.5$ mm, $v_t = 0.25$ m/s. (Nobel, 2013)

- Deflecting jet: (1) Deflecting jet happens when jet ratio $7.3 < p_j/su < 12$ and the jet traverse velocity $v_t > u_{f,v}$. $u_{f,v}$ is the soil vertical propagation

velocity, which is defined in Fig.2.6. (2) The soil cavity is shallower compared with penetrating jet, which is smaller than 2.5 times the nozzle diameter. (3) A soil wall with curving nerves texture is built, representing the deflection zone. (4) Limited amount of dislodged soil lumps can be found after the experiments.

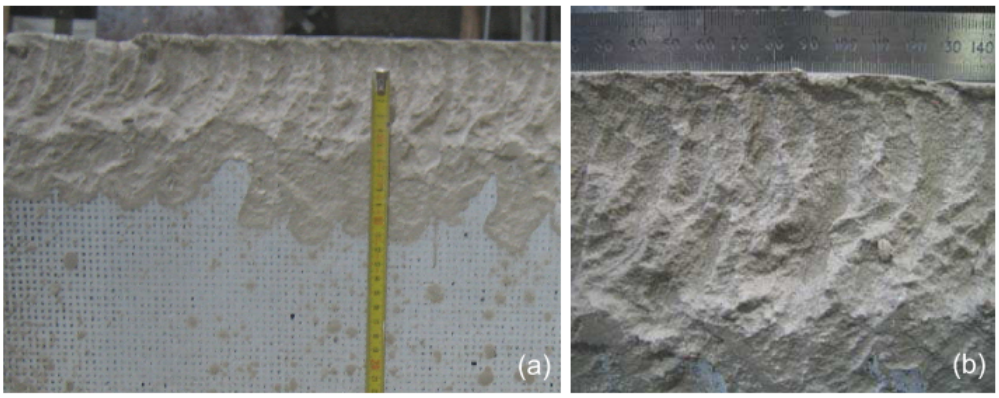

Figure 2.3: Deflecting jet: vertically oriented nerves in non-deflection zone. Test conditions: (a) $p_j/su = 25.8$, $D_n = 20$ mm, $v_t = 0.15$ m/s, (b) $p_j/su = 8.9$, $D_n = 5$ mm, $v_t = 1$ m/s. (Nobel, 2013)

- Dispersing jet: (1) Dispersing jet happens when jet ratio $5.4 < p_j/su < 7.3$ and the jet traverse velocity $v_t \gg u_{f,v}$. (2) The depth of the soil cavity is shallow while the width of the soil cavity is wider, which can be equal to 5 times the nozzle diameter. (3) The soil wall structure is irregular. (4) Dislodged soil lumps that can be found after the experiments.

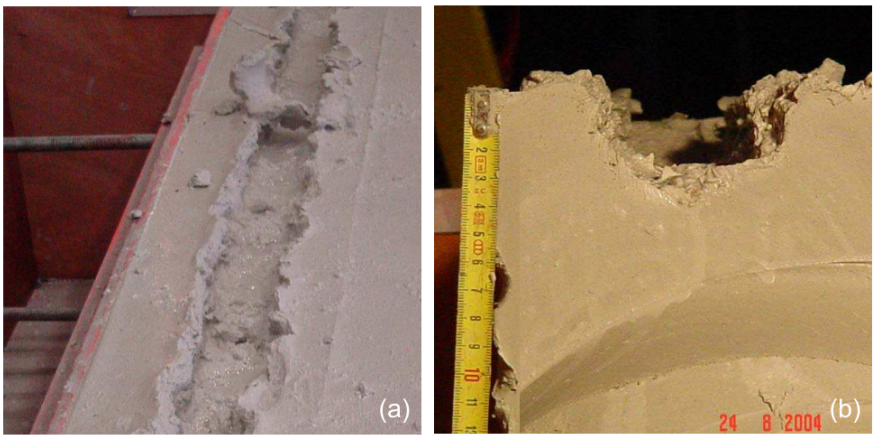

Figure 2.4: Dispersing jet: typical shallow soil cavity shape (a) top view, (b) transverse cross section. Test conditions: $p_j/su = 9$, $D_n = 32.5$ mm, $v_t = 1$ m/s. (Nobel, 2013)

- Hydro-fracturing: Hydro-fracturing happens when traverse velocity $v_t < 0.15$ m/s. The soil cavity dimensions are irregular. The soil fails at its weakest position.

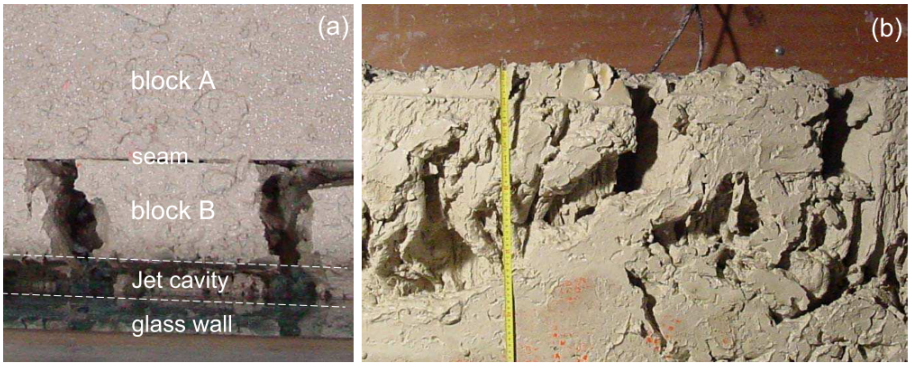

Figure 2.5: Hydro fracturing: (a) top view, with two planes of weaknesses along which the jet had penetrated the soil surface, (b) longitudinal cross section. Test conditions: $D_n = 32.5$ mm, $p_j = 0.82$ MN/m^2, $v_t = 0.125$ m/s, $su = 70$ kN/m^2. (Nobel, 2013)

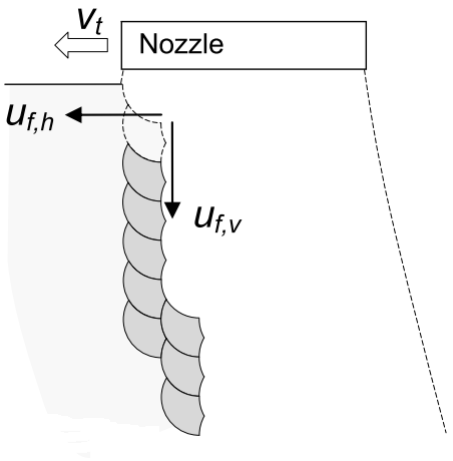

Figure 2.6: Definition of nozzle traverse velocity v_t, soil horizontal propagation speed $u_{f,h}$, soil vertical propagation speed $u_{f,v}$ (Nobel, 2013)

The penetrating jet and deflecting jet are the most relevant failure modes for the water injection dredging engineering.The penetrating jet and deflecting jet are the main objectives to be investigated in this thesis. The penetrating jet has two jet zones, which are non-deflection zone and deflection zone, see Fig.2.7. In the non-deflection zone of the penetrating jet, soil failure mechanism (a), see Fig.2.1, dominates. Pressure builds up on the surface of the soil until the jet stagnation pressure is over the shear strength of the soil. Then the soil is removed by the stagnation pressure of the jet. The smaller the jet ratio, the longer the duration of this process. When the traverse velocity of the nozzle is relatively low, the jet flow can follow a vertical line in the non-deflection zone as shown in Fig.2.7. As the traverse velocity of the jet is increasing, the jet flow in the non-deflection region will have an inclination angle as shown in Fig.2.7. The higher the jet traverse velocity, the larger the inclination angle will be. In the deflection zone of the penetrating jet, the jet flow will be deflected due to the traverse velocity of the jet and the resistance of the soil.

As the jet traverse velocity increases, the non-deflection zone will disappear, which is shown in Fig.2.8. This failure mode is called deflecting jet. The deflecting jet is comparable with the deflection zone of penetrating jet. The difference is the width of the soil strips. In deflecting jet, the jet flow can disperse freely in all

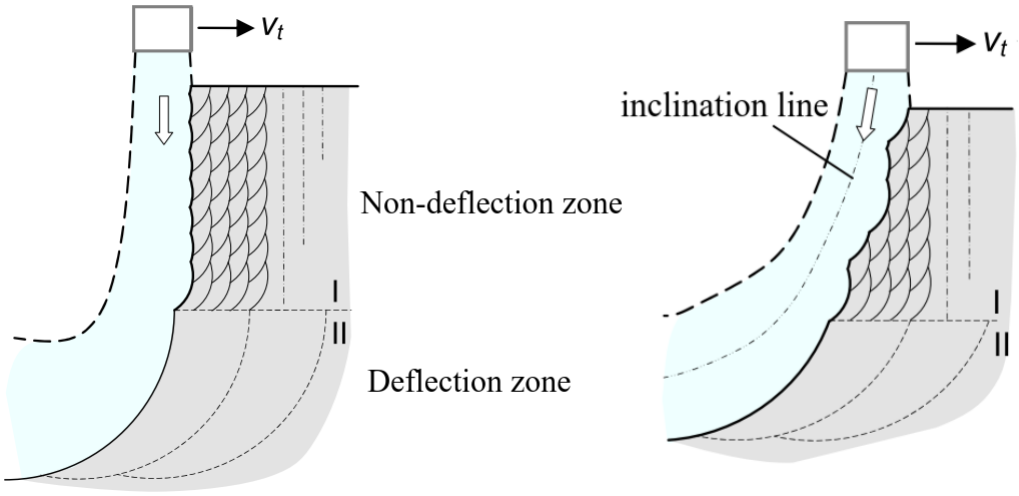

Figure 2.7: Definition of jet zones of penetrating jet. Zone I is the non-deflection zone, zone II is the deflection zone. When the jet traverse velocity is larger, jet flow follows a inclination line

direction. Differently, the jet flow in deflection zone of penetrating jet is hindered by the non-deflection zone. Therefore the the soil strips width of penetrating jet is equal to the soil cavity width.

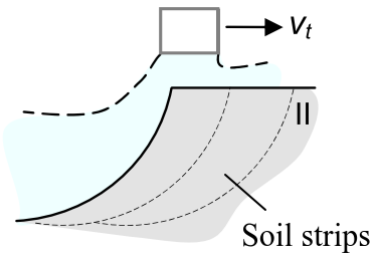

Figure 2.8: The definition of deflecting jet, which has only a deflection zone

Chapter 3

Modeling strategies

In this chapter, the modeling strategies used in this thesis will be introduced. The modeling of moving jet penetrating cohesive material can separate to three parts: moving jet modeling, soil modeling and sediment transport modeling. Besides, as the jet has a high inlet velocity and a high jet Reynolds number ($U_i D_n/\nu$, U_i is the jet inlet velocity, D_n is the nozzle diameter, ν is the kinetic viscosity of the fluid), the turbulence modeling is also needed. Dynamic mesh method AMI (arbitrary mesh interface) combined A/R (cell layer addition/removal)is applied modeling the moving jet. The drift-flux model is used for calculating the sediment transports. The cohesive soil clay is modeled as a Bingham plastic. Buoyant-$k-\epsilon$ model is used modeling turbulence.

3.1 Moving jet modeling

In this section, the moving jet modeling method will be introduced. The moving jet penetrating cohesive material is similar to a moving impinging jet. Before studying the moving impinging jet, the steady turbulent impinging jet is studied. Steady impinging jet CFD simulation has been done a lot in recent years. Table.3.1 shows the works of investigating the PTIJ (plane turbulent impinging jet) using RANS (Reynolds-averaged Navier–Stokes) models.

Table 3.1: Overview of CFD studies with RANS on PTIJ

Overview of CFD studies with RANS on PTIJ						
Authors	h/w	Re	turbulence model	results		Type of jet
				jet region	impinging region	
Jaramillo et al. (2008)	4, 9.2	20000	SKO, SKE	v, RMS	Nu	circular, plane
Jaramillo et al. (2012)	4, 9.2	20000	SKO, SKE, DNS	v, RMS	Nu	circular, plane
Angioletti et al. (2005)	4.5	1000 1500 4000	RNG, SST, RSM	v	Nu	circular
Seyedein et al. (1994)	2.5, 5, 7.5	$5000-20000$	LRKE, HRKE	v	p, Nu	plane
Craft et al. (1993)	2, 6	23000 70000	LRKE, RSM	v, RMS	Nu	circular
Park et al. (2003)	$0.5-4$	9800 11000 16400 20000 25100	SKO	v	Nu,C_f	plane
Kubacki and Dick (2010)	4, 9.2, 10	13500 20000	Hybrid SKO/LES, SKO	v, RMS	Reynolds stress, C_f, Nu	plane
Heyerichs and Pollard (1996)	2.6	10000	SKE, SKO		Nu, C_f	plane

Note: SKO means standard $k-\omega$ model, SKO means standard $k-\epsilon$ model, DNS means direct numerical simulation, RNG means Re-Normalization Group $k-\epsilon$ model, SST means SST $k-\omega$ model, RSM means Reynolds stress equation model, LRKE and HRKE means low and high Reynolds number $k-\epsilon$ model

Moving jet CFD simulation can only be found in Rahimi and Soran (2016) throughout published materials. Besides, only a moving inlet boundary condition is implemented in the study of Rahimi and Soran (2016) without modeling a real moving nozzle with geometry. It means that CFD modeling for a moving jet will be a challenge.

In this thesis, the moving jet modeling problem is solved using dynamic mesh AMI (arbitrary mesh interface) and A/R (cell layer addition removal). By combining AMI and A/R, a moving nozzle with real geometry is modeled instead of using a moving inlet boundary condition. The dynamic mesh algorithms used for modeling the moving jet will be introduced in section 4.4.

3.2 Soil modeling

Soil can be modeled as a solid following Hooke's law with a stress strain behavior or a fluid with a stress strain rate behavior. When describing the soil by a stress strain behavior, the deformation of soil can be regarded as a solid mechanics problem. FEM (finite element method)(Zienkiewicz et al., 2000) and FVM (finite volume method) (Cardiff et al., 2014) can both be used to solve the solid mechanics problem. In this study, the failure of the cohesive soil during jetting process is not only a deformation problem. The soils are first cut off and then fluidized by the jet flow. By modeling the soil with a stress strain behavior, the fluidization of the soil can not be simulated. Besides, CFD method is chosen in this thesis to study the fluid mechanics of the jet flow, a soil model with a stress strain rate behavior is relatively easier to be implemented into the CFD model. Therefore, the cohesive soil studied in this thesis is modeled as a fluid with a stress strain rate behavior. The non-Newtonian fluid model Bingham plastic model(Bingham, 1922), which can describe the cohesive material with a stress strain rate relation is applied in this thesis modeling the cohesive soil. In this section, the non-Newtonian fluid model Bingham plastic will be introduced.

For Newtonian fluid, the shear stress is linearly depending on the shear rate. The shear stress and shear rate of Newtonian fluid is described by using a constitutive equation:

$$\tau = \mu\dot{\gamma} \tag{3.1}$$

where τ is the shear stress, μ is the molecular viscosity, $\dot{\gamma}$ is the shear rate. In 1D case, the shear rate $\dot{\gamma}$ follows:

$$\dot{\gamma} = \frac{\partial u}{\partial y} \tag{3.2}$$

In 3D case, the shear rate should be expressed using shear rate tensor. Using Einstein notation, the shear rate tensor can be expressed as:

$$e_{ij} = \frac{1}{2}(u_{i,j} + u_{j,i}) \tag{3.3}$$

where e_{ij} is the shear rate tensor. The shear stress tensor τ_{ij} is calculated as:

$$\tau_{ij} = 2\mu(e_{ij} - \frac{1}{3}\Delta\delta_{ij}) \tag{3.4}$$

where Δ is given by:

$$\Delta = e_{\alpha,\alpha} = u_{\alpha,\alpha} \tag{3.5}$$

The fluid model used in this thesis for describing the cohesive soil clay is called Bingham plastic. A Bingham plastic (Bingham, 1922) can behave as solid or fluid in different load conditions. It behaves as a solid at low shear stress and viscous fluid at high shear stress. The threshold value of the shear stress used for determining if the Bingham plastic is in fluid or solid state is called yield stress τ_y. When the shear stress is larger than the yield stress τ_y, the Bingham plastic behaves as a viscous fluid. On the contrary, when the shear stress is lower than the threshold value τ_y, the Bingham plastic behaves as a solid. The Bingham plastic follows the following constitutive relation:

$$\tau = \tau_y + \eta\dot{\gamma} \tag{3.6}$$

where η is the plastic viscosity, $\dot{\gamma}$ is the shear rate. Fig.3.1 shows the behavior of Bingham plastic model compared with other constitutive models. If the yield stress τ_y of the Bingham plastic is zero, it becomes a Newtonian fluid.

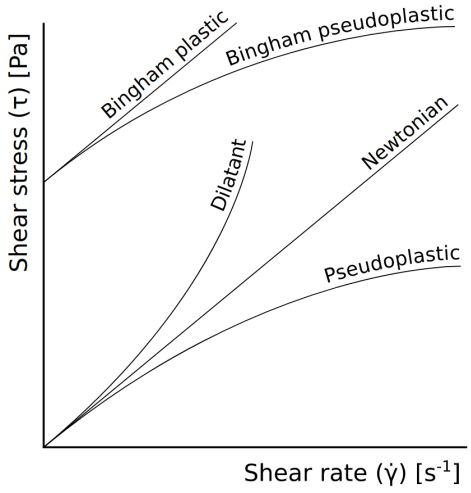

Figure 3.1: Shear stress and shear rate relationship of Newtonian fluid and non-Newtonian fluid

From the definition of shear stress and shear rate, Eq.(3.6) can also be written as:

$$\begin{aligned} \dot{\gamma} &= 0 \qquad\qquad when \quad \tau < \tau_y \\ \dot{\gamma} &= \frac{\tau - \tau_y}{\eta} \qquad when \quad \tau > \tau_y \end{aligned} \tag{3.7}$$

Eq.(3.7) is the Bingham plastic model in 1D. In 3D, shear rate is a second order tensor with magnitude:

$$\sqrt{\frac{1}{2}e_{ij}e_{ji}} = \sqrt{I_2} \tag{3.8}$$

where I_2 is the second invariant,

$$I_2 = \frac{1}{2}\left\{\left[\left(\frac{\partial u}{\partial x}\right)^2 + \left(\frac{\partial v}{\partial y}\right)^2 + \left(\frac{\partial w}{\partial z}\right)^2\right]\right. \tag{3.9}$$

$$\left. + \frac{1}{2}\left(\frac{\partial v}{\partial x} + \frac{\partial u}{\partial y}\right)^2 + \frac{1}{2}\left(\frac{\partial w}{\partial y} + \frac{\partial v}{\partial z}\right)^2 + \frac{1}{2}\left(\frac{\partial u}{\partial z} + \frac{\partial w}{\partial x}\right)^2\right\} \tag{3.10}$$

The 3D Bingham plastic model then becomes:

$$\tau_{ij} = \left(2\eta + \frac{\tau_y}{\sqrt{I_2}}\right) e_{ij} \tag{3.11}$$

The viscosity of the Bingham plastic is calculated from the definition of the Bingham plastic model Eq.(3.11):

$$\mu = \frac{\tau_y}{\sqrt{I_2}} + 2\eta \tag{3.12}$$

Yield stress is only applied in the soil regions. The soil regions are identified by the concentration field. After fluidization, the yield stress of the soil becomes zero. The yield stress is then defined as:

$$\tau_y = \begin{cases} \tau_y & when \quad \alpha_d > \alpha_t \\ 0 & when \quad \alpha_d < \alpha_t \end{cases} \tag{3.13}$$

where α_d is the concentration of the sediment phase, α_t is the threshold value for fluidization of soil.

3.3 Sediment transport modeling

The sediment suspensions consist of a carrier fluid and several sediment phases. The carrier fluid and sediment phases have certain volume concentration in the

sediment. This means the sediments can be described by the volume concentration of each content. Each sediment phase can be regraded as a continuum with certain density and viscosity. The motion of each phase can be described and solved numerically using separated continuity and momentum equations. This method is called Euler/Euler method, which is used often for solving multiphase flow problems. The computational cost of this method is limited when solving two or three phases flow. However, when dealing with multiple phases flow, the computational cost becomes prohibitively large. In dredging industry, the transported sediment always consists of multiple fractions or phases. Therefore the computational cost of the Euler/Euler method becomes unacceptable. Besides, in Euler/Euler method, the coupling forces between phases need to be modeled. When dealing with multiple phases, the coupling forces between phases cannot be easily modeled.

Another approach which can be used to solve the sediments transport is called CFD-DEM (Computational Fluid Dynamics / Discrete Element Method) model (Tsuji et al., 1993). CFD-DEM model can be used to model or simulate systems combining fluids with solids or particles. In CFD-DEM, the motion of discrete solids or particles phase is obtained by the DEM which applies Newton's laws of motion to every particle, while the flow of continuum fluid is solved by using CFD approach. The DEM model needs to be solved by using GPU (graphics processing unit), while the CFD model is solved by CPU (central processing unit). As the limitation of GPU power, this method is not used in this thesis.

An alternative approach is called drift-flux model, which is a simplification of the Euler/Euler model. In drift-flux model, the momentum equation for each phase is summed, yielding one momentum equation which describes the motion of the mixture flow. Therefore, the number of continuity and momentum equations are limited which saves computational power. As the lower computational cost and its sufficiency for predicting the sediment transport , drift-flux model is chosen modeling the sediment transport in this thesis. Derivation of drift-flux model can be seen in Zuber and Findlay (1965), Drew (1983), Manninen et al. (1996), Hiltunen et al. (2009), Ishii and Hibiki (2010), Jakobsen (2014) and Goeree et al. (2016). In the following section, a short derivation of the drift-flux model will be

shown.

3.3.1 Governing equations

The governing equations of drift-flux model will be explained in this section. A detailed derivation of the drift-flux model is shown in Appendix A.

Mixture continuity equation

The mixture continuity equation is:

$$\frac{\partial \rho_m}{\partial t} + \nabla \cdot (\rho_m \mathbf{u}_m) = 0 \tag{3.14}$$

where ρ_m is the mixture density, $\mathbf{u}_m$ is the mixture velocity vector.

Mixture momentum equation

The mixture momentum equation is:

$$\begin{aligned} &\frac{\partial \rho_m \mathbf{u}_m}{\partial t} + \nabla \cdot \rho_m \mathbf{u}_m \mathbf{u}_m = \\ &- \nabla p_m + \nabla \cdot (\mathbf{T}_m + \mathbf{T}_m^t - \sum_{k=1}^{N} \alpha_k \rho_k \mathbf{u}_{km} \mathbf{u}_{km}) + \rho_m \mathbf{g} \end{aligned} \tag{3.15}$$

where p_m is the mixture pressure, $\mathbf{T}_m$ and $\mathbf{T}_m^t$ are viscous and turbulent shear stress tensors of mixture. $\mathbf{g}$ is the gravitational acceleration vector. α_k is the volume fraction of phase k. $\mathbf{u}_{km}$ is the velocity difference between mixture and phase k.

Phase transport equation

The closure of the concentration term α_k in the mixture momentum equations is accomplished by using phase transport equation:

$$\frac{\partial \alpha_k}{\partial t} + \nabla \cdot (\mathbf{u}_k \alpha_k) = 0 \tag{3.16}$$

3.4 Turbulence modeling

As the jet used in this thesis has a high inlet velocity (around $30m/s$) and high jet Reynolds number, turbulence modeling is needed. From the literature study in section 3.1, RANS model has the ability to simulate the turbulent jet. Turbulence modeling is the construction and use of a mathematical model to predict the effects of turbulence. Without turbulence modeling, capturing the turbulence using DNS (Direct Numerical simulation) needs very small mesh size and small time step, in other words, huge computational power. Therefore, using DNS for engineering application is not cheap. In order to reduce the computational cost, turbulence modeling is employed. LES (Large Eddy Simulation) and RANS (Reynolds Averaged Navier Stokes) model are widely used turbulence modeling methods. In this thesis, a buoyancy $k - \epsilon$ RANS model is used for turbulence modeling.

3.4.1 Averaging method

RANS models use time averaged or ensemble method defining the turbulence. The turbulent terms can be modelled as:

$$\phi = \bar{\phi} + \phi' \tag{3.17}$$

where $\bar{\phi}$ is the time averaged value, ϕ' is the fluctuating value. The averaged term $\bar{\phi}$ is defined as:

$$\bar{\phi} = \frac{1}{T}\int_0^T \phi dt \quad or \quad \frac{1}{N}\sum_i \phi_i \tag{3.18}$$

where i is the experiment number. The fluctuation term ϕ' has the following property:

$$\int_0^T \phi' dt = 0 \tag{3.19}$$

In drift-flux model, using RANS model, the velocity $\mathbf{u}$ and pressure p can be described as:

$$\mathbf{u} = \bar{\mathbf{u}} + \mathbf{u}' \quad p = \bar{p} + p' \tag{3.20}$$

Substitute these into continuity and momentum equation of Navier Stokes equation, and take an time average of those equations. The continuity and momentum will become:

$$\nabla \cdot \bar{\mathbf{u}} = 0 \tag{3.21}$$

$$\frac{\partial \bar{\mathbf{u}}}{\partial t} + \nabla \cdot \bar{\mathbf{u}}\bar{\mathbf{u}} = -\frac{1}{\rho}\nabla \bar{p} + \nabla \cdot (\mathbf{T} + \mathbf{T}^t) \tag{3.22}$$

The $\mathbf{T}$ and $\mathbf{T}^t$ term are the viscous shear stress and Reynolds stress. The Reynolds stress term is given as:

$$\mathbf{T}^t = -\overline{u_i' u_j'} \tag{3.23}$$

When $i = j$, this term behaves as a normal stress. When $i \neq j$, it behaves as a shear stress. The existence of Reynolds stress term means a non-closure problem. This term will be closed by using buoyant $k - \epsilon$ model. The buoyant $k - \epsilon$ model will be introduced in the next section.

3.4.2 Buoyant $k - \epsilon$ model

Buoyant $- k - \epsilon$ model is similar to the $k - \epsilon$ model, which has both turbulent kinetic energy k and dissipation rate ϵ. The reason why *buoyant* $- k - \epsilon$ is chosen refers to the modulation of turbulent kinetic energy caused by density stratification effects is incorporated in this model. The turbulent kinetic energy is defined as:

$$k = \frac{1}{2}({u_1'}^2 + {u_2'}^2 + {u_3'}^2) \tag{3.24}$$

The Reynolds shear stress term is modelled as:

$$-\overline{u_i' u_j'} = \nu_t(\frac{\partial \overline{u_i}}{\partial x_j} + \frac{\partial \overline{u_j}}{\partial x_i}) - \frac{2}{3}k\delta_{ij} \tag{3.25}$$

where k is the turbulent kinetic energy, δ_{ij} is the Kronecker δ (δ_{ij}=1 for $i = j$, δ_{ij}=0 for $i \neq j$). ν_t is the turbulence eddy viscosity which is modelled as:

$$\nu_t = C_\mu \frac{k^2}{\epsilon} \tag{3.26}$$

Two new variable turbulence kinetic energy k and and turbulence dissipation rate ϵ are created, it means two new equations are needed to close this problem. Transport equation of k and ϵ are used to close this problem:

$$\frac{\partial k}{\partial t} + \nabla \cdot (\mathbf{u}k) = \nabla \cdot (\nu + \frac{\nu_t}{\sigma_k}\nabla k) + P_k + G_k - \rho\epsilon \tag{3.27}$$

$$\frac{\partial \epsilon}{\partial t} + \nabla \cdot (\mathbf{u}\epsilon) = \nabla \cdot (\nu + \frac{\nu_t}{\sigma_\epsilon}\nabla \epsilon) + C_{1\epsilon}\frac{\epsilon}{k}(P_k + G_k - C_{3\epsilon}G_k) - C_{2\epsilon}\frac{\epsilon^2}{k} \tag{3.28}$$

where P_k is the production of turbulence kinetic energy k, which is given by:

$$P_k = \nu_t(\frac{\partial \overline{u_i}}{\partial x_j}\frac{\partial \overline{u_j}}{\partial x_i})\frac{\partial \overline{u_i}}{\partial x_j} \tag{3.29}$$

and G_k is the buoyancy production/destruction of k, which is given by:

$$G_k = \frac{g_i}{\rho_r}\frac{\nu_t}{\sigma_t}\frac{\partial \rho}{\partial x_i} \tag{3.30}$$

C_{mu}, σ_k, σ_ϵ, $C_{1\epsilon}$, $C_{2\epsilon}$ and $C_{3\epsilon}$ are constant values gathered from experiment. The value of these terms are shown in Table:

parameters in buoyant $k - \epsilon$ model

C_ν	$C_{1\epsilon}$	$C_{2\epsilon}$	$C_{3\epsilon}$	σ_k	σ_ϵ	σ_t
0.09	1.44	1.92	0.8	1.0	1.3	1.0

Physically, turbulence model should not be applied to the soil, which does not move before fluidizing to sediment suspensions. Therefore a concentration limitation for the eddy viscosity ν_t is applied to the turbulence model. The eddy viscosity of the flow follows:

$$\nu_t = \begin{cases} 0 & when \quad \alpha_d > \alpha_{tur} \\ \nu_t & when \quad \alpha_d < \alpha_{tur} \end{cases} \tag{3.31}$$

where α_d is the volume concentration of the sediment, α_{tur} is the threshold value determining if the turbulence eddy viscosity is applied. To start the calculation, the initial and boundary conditions also need to be applied to the turbulence kinetic energy k and dissipation rate ϵ. The initial condition for turbulent kinetic energy is calculated as:

$$k = \frac{3}{2}(UI)^2 \tag{3.32}$$

where U is the mean flow velocity and I is the turbulence intensity. For dissipation rate ϵ:

$$\epsilon = C_\mu \frac{k^{\frac{3}{2}}}{l} \tag{3.33}$$

where C_μ has a constant value, which always equals to 0.09. l is the turbulent length scale. For calculating jet inlet situations, l is calculated as $l = 0.015D_n$(Jaramillo et al., 2012).

To resolve the turbulence boundary layer near the wall, a prohibitively large number of grid points would be required. To get rid of huge amount of grid points near the wall and save computational power, wall functions are used. The wall functions follow the 'law of the wall'(Wilcox et al., 1998), see Fig.3.2. The value of y^+ at the first grid cell from the wall should follow $30 < y^+ < 300$. If y^+ is too low, the model is invalid. If y^+ is too high, the wall is not properly resolved.

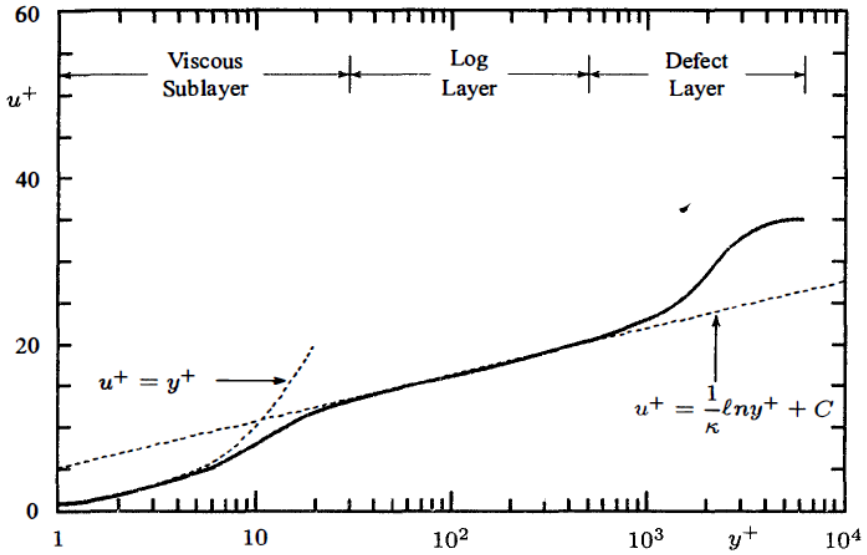

Figure 3.2: Typical velocity profile for a turbulent boundary layer(Wilcox et al., 1998). $y^+ = yu_\tau/\nu$, $u^+ = u/u_\tau$. y is the distance from the wall to the center of the first grid-cell from the wall. u_τ is the wall friction velocity. ν is the kinetic viscosity of the fluid. u is the flow velocity.

Chapter 4

Numerical techniques

The Navier Stokes equations are partial differential equations, which do not have a analytical solution till today. The most common way to solve it is using numerical discretization approaches. The drift-flux model used in this thesis is composed of several Navier Stokes like equations, which also have no analytical solution. Three widely used discretization methods are FDM (Finite Difference Method), FEM (Finite Element method) and FVM(Finite Volume Method). FVM is used in this thesis study, which is available in OpenFOAM(Greenshields, 2018). The solution algorithm of drift-flux model used in OpenFOAM is based on PIMPLE algorithm, which is a combination of PISO (Pressure Implicit with Splitting of Operator) and SIMPLE (Semi-Implicit Method for Pressure-Linked Equations). Collocated grids, which save all variables (e.g. pressure, velocity, density and concentration) at the cell center, are used instead of staggered grids. Collocated method suffers velocity pressure coupling problem resulting an oscillating solution. To prevent this, Rhie and Chow's method is used (Rhie and Chow, 1983). Besides, to model the moving jet, dynamic mesh algorithms AMI (arbitrary mesh interface) and A/R (cell layer addition/removal) are used. In this chapter, the numerical techniques used in this thesis will be introduced.

4.1 Discretization methods and numerical schemes

The discretization method used in this thesis is called FVM (Finite Volume Method). In FVM, the computational domain is divided into a finite number of CV (control volumes). The variables can be saved at both the center and boundary of CV. In the drift-flux solver of OpenFOAM, collocated grids method is used, the variables are all saved on the center of CV. The rate of change of variables (the $\partial\phi/\partial t$ term, ϕ means variable) are calculated by the fluxes over the surface of CV at each time step. These fluxes are determined by both the convection and diffusion term of the partial differential equations. The fluxes at the cell surface is calculated by doing interpolation with the neighbour cells. If the cells are located at the boundary, the fluxes will be determined by the boundary conditions. The details of the finite volume methods can be found in Ferziger and Peric(Ferziger and Peric, 2012).

4.1.1 Discretization of Navier Stokes equations

In OpenFOAM, the Navier Stokes equations are discretized on collocated grid instead of staggered grid. Even collocated grid has results oscillating problem compared with staggered method, it still has the following advantages(Wesseling, 2001):

- It is relatively easy to extend collocated scheme to a structured curvilinear grid in Cartesian reference frame compared with staggered arrangement.
- Solving compressible Navier Stokes equations favors collocated grid better than staggered grid.
- The most efficient way to solve linear system is based on solving momentum and pressure correction equations. Using the momentum and pressure correction equations needs hierarchical algorithms like e.g. multigrid. This can be easily done by using collocated grid while the grid arrangement in staggered grid is difficult.

In the following part of this section, the discretization of Navier Stokes equations on collocated grid will be explained.

Collocated grid

In collocated grid method, the unknowns are saved collocated with respect to each other at the cell center. The arrangement of the unknowns in a 2D cell is shown in Fig.4.1.

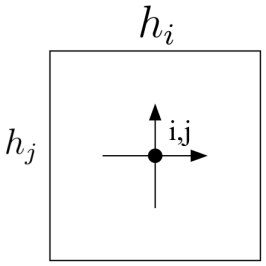

Figure 4.1: 2D unknowns arrangement in collocated grid on cell Ω_{ij}, $\rightarrow$ and $\uparrow$ mean the vector field e.g. velocity, $\bullet$ means the scalar field e.g. pressure, i, j represent the index of the cell

In later part of this section, a 2D discretization based on collocated grid of Navier Stokes in Cartesian coordinate system will be explained.

Discretization of continuity equation on collocated grid

Using FVM to continuity equation on cell Ω_{ij}:

$$\int_{\Omega_{ij}} u_{\alpha,\alpha} d\Omega = \oint_{\partial\Omega_{ij}} u_\alpha n_\alpha dS = h_j u_1|_{i-1/2,j}^{i+1/2,j} + h_i u_2|_{i,j-1/2}^{i,j+1/2} \tag{4.1}$$

where central interpolation is used to $u_1|_{i+1/2,j}$ and $u_2|_{i,j+1/2}$:

$$\begin{aligned} u_1|_{i+1/2,j} &= \frac{u_1|_{i,j} + u_1|_{i+1,j}}{2} \\ u_2|_{i,j+1/2} &= \frac{u_2|_{i,j} + u_2|_{i,j+1}}{2} \end{aligned} \tag{4.2}$$

Discretization of momentum equation on collocated grid

The momentum equation can be described as:

$$u_{\alpha,t} + (u_\alpha u_\beta),_\beta = -p_{,\alpha} + Re^{-1} u_{\alpha,\beta\beta} + f_\alpha^\beta \tag{4.3}$$

Move the RHS terms to the LHS and take the volume integration in Ω_{ij}:

$$\begin{aligned}
&\int_{\Omega_{ij}} [u_{\alpha,t} + (u_\alpha u_\beta),_\beta + p_{,\alpha} - Re^{-1} u_{\alpha,\beta\beta} - f_\alpha^b] d\Omega_{ij} \\
=&\int_{\Omega_{ij}} [(u_\alpha u_\beta + \delta_{\alpha\beta} p - Re^{-1} u_{\alpha,\beta}),_\beta] d\Omega_{ij} + h_i h_j (u_{\alpha,t} - f_\alpha^b)_{i,j} \\
=&h_j (u_\alpha u_1 + \delta_{\alpha 1} p + Re^{-1} u_{\alpha,1})\big|_{i-1/2,j}^{i+1/2,j} + h_i (u_\alpha u_2 + \delta_{\alpha 2} p + Re^{-1} u_{\alpha,2})\big|_{i,j-1/2}^{i,j+1/2} \\
&+ h_i h_j (u_{\alpha,t} - f_\alpha^b)_{i,j} = 0
\end{aligned} \tag{4.4}$$

The derivatives are approximated as follows:

$$\begin{aligned}
u_{\alpha,1}|_{i+1/2,j} &= \frac{u_\alpha|_{i+1,j} - u_\alpha|_{i,j}}{h_i} \\
u_{\alpha,2}|_{i,j+1/2} &= \frac{u_\alpha|_{i,j+1} - u_\alpha|_{i,j}}{h_j}
\end{aligned} \tag{4.5}$$

The inertia terms are approximated by using central interpolation as follows:

$$\begin{aligned}
u_1^2|_{i+1/2,j} &= \frac{u_1^2|_{i,j} + u_1^2|_{i+1,j}}{2} \\
(u_1 u_2)|_{i,j+1/2} &= \frac{(u_1 u_2)|_{i,j} + (u_1 u_2)|_{i,j+1}}{2}
\end{aligned} \tag{4.6}$$

The pressure term is also interpolated using central scheme:

$$p_{i+1/2,j} = \frac{p_{i,j} + p_{i+1,j}}{2} \tag{4.7}$$

The stencil of collocated grid is shown in Fig.4.2.

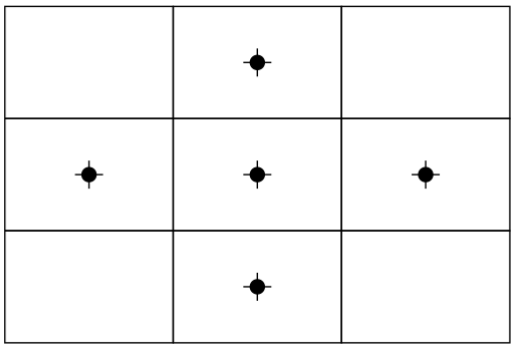

Figure 4.2: Stencil of collocated grid in 2D, − and | mean velocity, • means pressure

4.1.2 Numerical schemes

When simulating sediment transport using drift-flux model, it is important to prevent negative values in the solution of sediment concentrations. A negative value of concentration, which can be caused by numerical fluctuations is not physically possible. To prevent the numerical oscillation, a certain class of interpolation schemes does not suffer from negative values in the outcome of the numerical solution can be used. These schemes are called Total Variational Diminishing schemes (TVD). TVD schemes are monotone and second-order accurate and make use of so-called flux limiters. In this thesis the van Leer flux limiter is used, see Van Leer (1974). This numerical scheme is applied to the concentration convection terms in momentum equations of drift-flux model to prevent a negative value of concentration. Central scheme, which is introduced and applied in section 4.1 has been implemented to other terms during the simulation.

Besides, to prevent numerical diffusion, `local min` scheme is implemented to the diffusion term in the momentum equation of drift-flux model. The `local min` scheme follows:

$$\phi_{i+1/2,j} = min(\phi_{i,j}, \phi_{i+1,j}) \quad \phi_{i,j+1/2} = min(\phi_{i,j}, \phi_{i,j+1}) \tag{4.8}$$

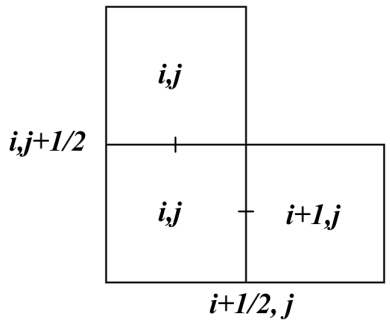

Figure 4.3: Definition of `local min` scheme.

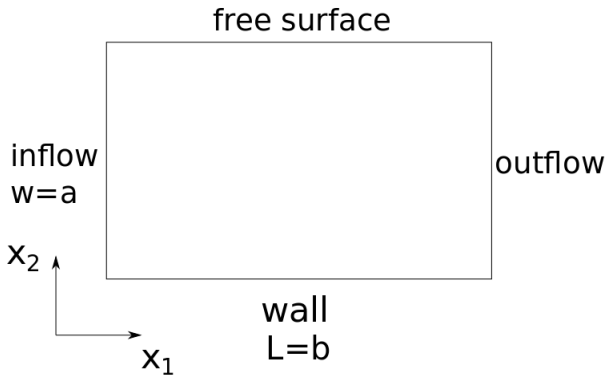

Figure 4.4: Boundary condition set up for explanation, inflow condition is applied to the left, outflow condition is applied to the right, no-slip condition is applied on the bottom, free surface condition is applied on the top. The domain has a width of $w = a$ and length of $L = b$

4.2 Boundary conditions

There are several boundary conditions which are mostly used in CFD simulations, which are no-slip, free surface, inflow and outflow boundary conditions. These boundary conditions will be explained in this section. To explain the boundary conditions, a boundary set up shown in Fig.4.4 is used.

No-slip wall conditions

When the viscous fluid is flowing along the solid wall, it has no relative velocity between the fluid and wall. At the solid surface, it follows:

$$\mathbf{u}(t, \mathbf{x}) = \mathbf{v}(t, \mathbf{x}) \tag{4.9}$$

where $\mathbf{u}$ is the fluid velocity, $\mathbf{v}$ is the local wall velocity. No-slip wall boundary condition is a Dirichlet boundary condition seen from Eq.(4.9).

Free surface conditions

The free surface boundary condition implies the tangential stress components at the free surface are zero. To simply introduce this, a free surface boundary condi-

tion is applied at $x_2 = a$ in Fig.(4.4). At the free surface, the normal velocity and tangential shear rate is zero:

$$u_2(t, x_1, x_2 = a) = 0, \quad u_{1,2}(t, x_1, x_2 = a) = 0 \tag{4.10}$$

Dirichlet boundary condition is applied to the normal velocity u_2 and Neumann boundary condition is applied to the tangential shear rate $u_{1,2}$.

Inflow conditions

In Fig.4.4, an inflow boundary condition is applied to the left boundary $x_1 = 0$. The inflow condition is a Dirichlet boundary condition:

$$u_1(t, x_1 = 0, x_2) = U_1(t, x_1 = 0, x_2), \quad u_2(t, x_1 = 0, x_2) = U_2(t, x_1 = 0, x_2) \tag{4.11}$$

where U_1 and U_2 are the prescribed velocity by the inflow condition defined by user.

Outflow conditions

The physical information of the outflow boundary is often not enough. Usually, only the pressure is known. To get rid of spurious numerical wiggles, an artificial outflow boundary condition, which apply homogeneous Neumann boundary condition for tangential velocity is always used. The outflow boundary condition at $x_1 = b$ in Fig.4.4 is:

$$p(t, x_1 = b, x_2) = p_\infty, \quad u_{2,1}(t, x_1 = b, x_2) = 0 \tag{4.12}$$

4.3 Solution algorithms

Three solution algorithms, which are available in OpenFOAM, will be introduced here. The three algorithms are SIMPLE (Semi-Implicit Method for Pressure-Linked Equations), PISO (Pressure Implicit with Splitting of Operators) and PIMPLE (a combination of SIMPLE and PISO). In this thesis, solver `driftFluxDyMFoamv1812` uses PIMPLE algorithm.

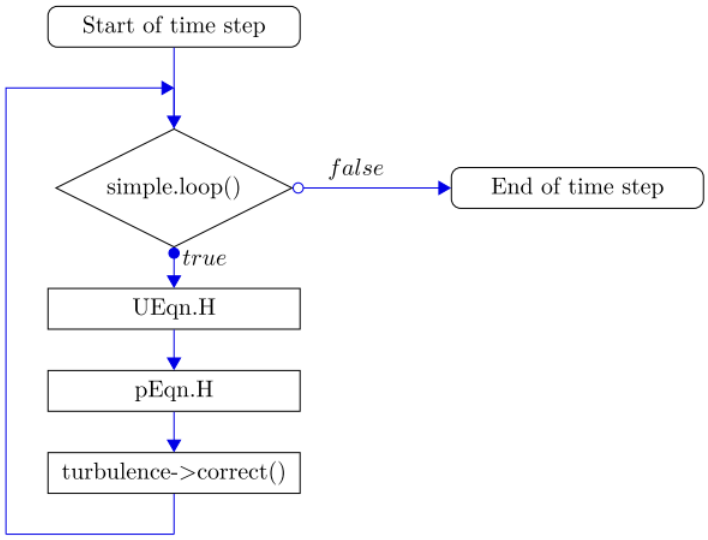

Figure 4.5: Flow chart of SIMPLE algorithm(Holzinger, 2015)

SIMPLE

In OpenFOAM, SIMPLE algorithm predicts the velocity using `UEqn.H` and then corrects both pressure and velocity using `pEqn.H`. This procedure repeats till a convergence criteria is reached. The solving procedure is shown in Fig.4.5. The solving procedure can be described as:

1) Check convergence using `simple.loop()`
2) Predict velocity using momentum predictor in `UEqn.H`
3) Correct both pressure and velocity using pressure corrector and velocity corrector in `pEqn.H`
4) Solve turbulence model using `turbulence->correct()`
5) Repeat 1) to 4).

In SIMPLE algorithm, the rate of change $\partial\phi/\partial t$ term is not solved. The Navier Stokes equations solved by SIMPLE is:

The continuity equation:

$$\nabla \cdot \mathbf{u} = 0 \tag{4.13}$$

The Momentum equation:

$$\nabla \cdot (\mathbf{uu}) - \nabla \cdot \nu \nabla \mathbf{u} = -\nabla p \tag{4.14}$$

The discretized form of the momentum equations, which is used as the momentum corrector in `UEqn.H` can be described as:

$$\mathbf{M} \cdot \mathbf{u} = -\nabla p \tag{4.15}$$

The $\mathbf{M} \cdot \mathbf{u}$ term can be separated as:

$$\mathbf{M} \cdot \mathbf{u} = \mathbf{A} \cdot \mathbf{u} - \mathbf{H} \tag{4.16}$$

where matrix $\mathbf{A}$ is a diagonal matrix with the value of diagonal of matrix $\mathbf{M}$. Substitute Eq.(4.16) into Eq.(4.15):

$$\mathbf{A} \cdot \mathbf{u} - \mathbf{H} = -\nabla p \tag{4.17}$$

The momentum corrector in *pEqn.H* can then be derived:

$$\mathbf{u} = \mathbf{A}^{-1} \cdot (\mathbf{H} - \nabla p) \tag{4.18}$$

Take a divergence of Eq.(4.18) and apply continuity equation, the pressure corrector in `pEqn.H` can be derived:

$$\nabla \cdot (\mathbf{A}^{-1} \cdot \nabla p) = \nabla \cdot (\mathbf{A}^{-1} \cdot \mathbf{H}) \tag{4.19}$$

PISO

PISO solves the rate of change term which SIMPLE does not solve. The momentum equation in PISO algorithm is:

$$\frac{\partial \mathbf{u}}{\partial t} + \nabla \cdot (\mathbf{uu}) - \nabla \cdot \nu \nabla \mathbf{u} = -\nabla p \tag{4.20}$$

In PISO algorithm, the velocity is first predicted by `UEqn.H`. Then, go through `piso.loop` and correct velocity and pressure using pressure corrector and velocity corrector in `pEqn.H` until the residual tolerance is reached. The solving procedure is shown in Fig.4.6. The solving procedure can be described as:

1) Predict velocity using momentum predictor in `UEqn.H`
2) Check convergence using `piso.loop()`

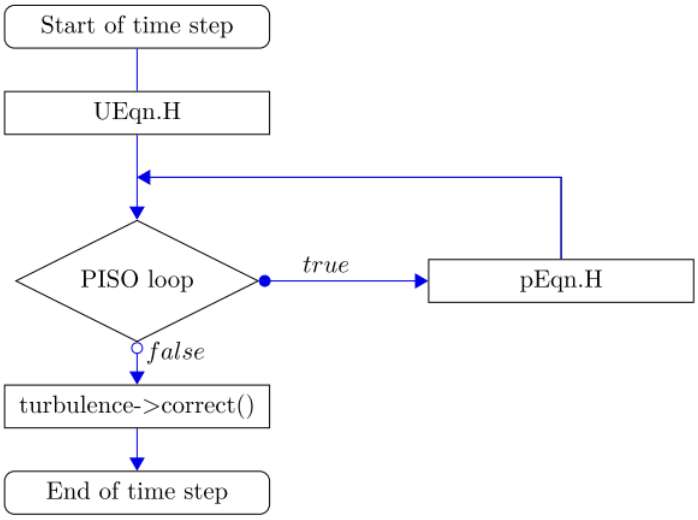

Figure 4.6: Flow chart of PISO algorithm(Holzinger, 2015)

3) Correct both pressure and velocity using pressure corrector and velocity corrector in `pEqn.H`.
4) Solve turbulence model using `turbulence->correct()`
5) Repeat 1) to 4).

PIMPLE

PIMPLE algorithm is a combination of SIMPLE and PISO. The solving procedure is shown in Fig.4.7. The solving preocedure can described as:

1) Check convergence using `pimple.loop()`
2) Predict velocity using momentum predictor in `UEqn.H`
3) Correct both pressure and velocity using pressure corrector and velocity corrector in `pimple.correct()`.
4) Solve turbulence model using `turbulence->correct()`
5) Repeat 1) to 4).

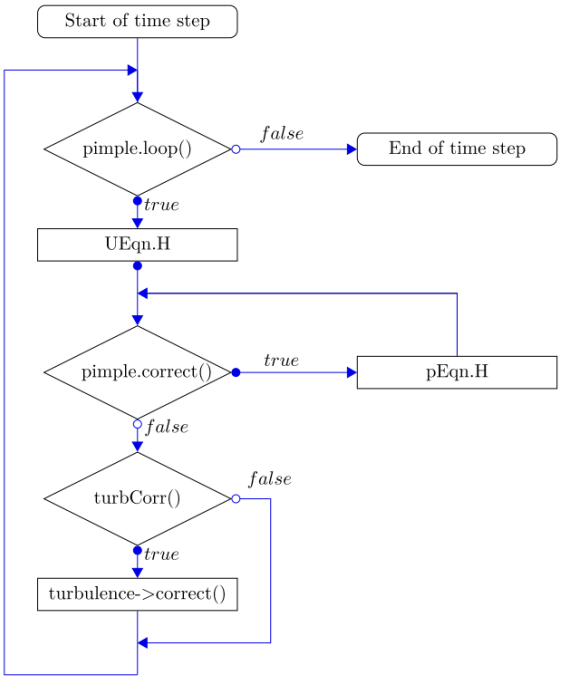

Figure 4.7: Flow chart of PIMPLE algorithm(Holzinger, 2015)

4.4 Dynamic mesh algorithms

When a moving object is appearing in the simulation, dynamic mesh can be a solution for this kind of problem. In this thesis, a moving jet has to be studied, which can be modelled by using dynamic mesh. Two main dynamic mesh concepts which are AMI (arbitrary mesh interface) and A/R (cell layer additional removal) have been used. In this section, the dynamic mesh algorithm used in this thesis will be introduced.

4.4.1 Basic equations for dynamic mesh

In this thesis, *OpenFOAM*(Greenshields, 2018), a CFD software based on FVM (finite volume method), is used for simulation. Therefore, when using dynamic mesh algorithm, the actual moving part of the mesh is the volume. The dynamic

mesh algorithm for FVM follows Eq.(4.21):

$$\frac{\partial}{\partial t}\int \rho\phi\partial V + \oint \rho\mathbf{n}\cdot(\mathbf{u}-\mathbf{u_s})\phi\partial S - \oint \rho\gamma_\phi\mathbf{n}\cdot\nabla\phi\partial S = \int s_\phi\partial V \tag{4.21}$$

In Eq.(4.21), ϕ is the transport property (e.g. velocity, temperature), ρ is the density of the transport property, $\mathbf{n}$ is the unit normal factor of the boundary surface of the control volume, $\mathbf{u}$ is the velocity vector of the fluid, $\mathbf{u_s}$ is the velocity of the boundary surface of the moving mesh, γ_ϕ is the diffusion coefficient, s_ϕ is the volume source term. Relationship between the change rate of volume V and boundary surface S velocity $\mathbf{u_s}$ is defined by SCL (space conservation law)(Demirdzic and Peric, 1988) in Eq.(4.22).

$$\frac{\partial}{\partial t}\int \partial V = \oint \mathbf{n}\cdot\mathbf{u_s}\partial S \tag{4.22}$$

4.4.2 Topological change dynamic mesh

The lowest mesh topological change is called primitive mesh operations. Primitive mesh operations can add, remove or (connect) modify a point, a face or a cell on the mesh. It allows user to completely collapse an existing mesh or to build a mesh starting from empty space. Primitive mesh operations are flexible but tedious and impractical to use. For example, a single primitive mesh operation for a point, face or cell may lead to an invalid mesh. Therefore, primitive mesh changes need to be executed in batches.

The second level of mesh topological changes is called mesh modifier. Mesh modifier is executed based on primitive mesh operations. It holds s self-contained definition and a triggering mechanism. For example, the cell layer addition/removal which is going to be used in the thesis. The triggering mechanism for this is the thickness of the cell layer. When the thickness of the cell layer is larger than the user-defined limitation, a new layer will be added. Vice versa, when the layer thickness is lower than the limitation, the cell will be removed. In *OpenFOAM*(Greenshields, 2018), the following mesh modifiers are now available.

- Cell layer addition/removal;

- Attach-detach boundary;
- Sliding interface(which is called AMI in *OpenFOAM*);
- Dynamic crack propagation in non-linear structural analysis;
- Regular octree mesh refinement for hexahedral mesh regions.

Cell layer addition/removal(Greenshields, 2018) and AMI(Farrell and Maddison, 2011)(Farrell et al., 2009)(Menon and Schmidt, 2011) will be used in this thesis for simulating the moving jet. In the following sections, these two dynamic mesh algorithms will be introduced.

AMI - Arbitrary Mesh Interface

Arbitrary mesh interface is similar as the sliding interface and the general grid interface (GGI)(Beaudoin and Jasak, 2008). Sliding interface topology modifier allows for the dynamic stitching and splitting of mesh regions with different mesh structures. It generates seamless joint, therefore no special numerical methods are needed to solve the equations across the interface. This is different from AMI, because AMI is solving two topologically separated mesh by interpolating the flux among the surface using weighting factors. In AMI, the interpolation of flux is taking place at the inner boundary of the outer domain and outer boundary of the inner domain. The interpolation method is a conservative interpolation method called local Galerkin projection(Farrell and Maddison, 2011). The sliding interface and AMI algorithm are shown in Fig.4.9 and Fig.4.8 below.

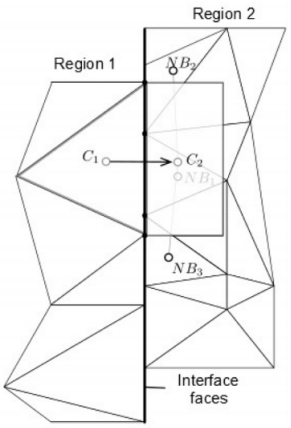

Figure 4.8: AMI interpolation between interface(Mangani et al., 2014), where NB means the neighbour point, C is cell under consideration

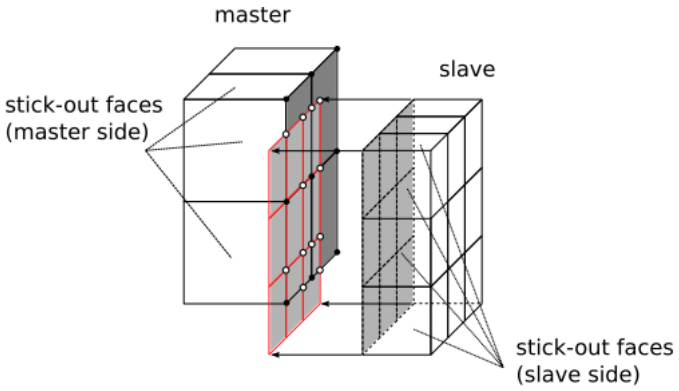

Figure 4.9: Stitching and splitting of mesh in sliding mesh algorithm(Piscaglia et al., 2014)

A/R - Cell layer addition/removal

A/R (cell layer addition/removal) is a dynamic mesh algorithm, modifying mesh by adding and removing cell layers when the mesh is moving. When mesh is modifying, the majority of the mesh remains fixed, while only parts of the mesh layers are added or removed. This property of A/R allows keeping the mesh

quality (both size and shape of the mesh) constant during the simulation. Mesh layer thickness needs to be monitored during simulation. Two threshold values, which are maximum and minimum mesh layer thickness need to be set up before starting the simulation. During the simulation, for every time step, these two thresholds will be checked up. When the cell layer thickness is over the maximum value, new cell layers will be added. However, cell layers will be removed while the layer thickness decreases to the minimum value. This dynamic mesh algorithm is valid in *OpenFOAM* (Greenshields, 2018). Fig.4.10 and Fig.4.11 show how A/R dynamic mesh algorithm works.

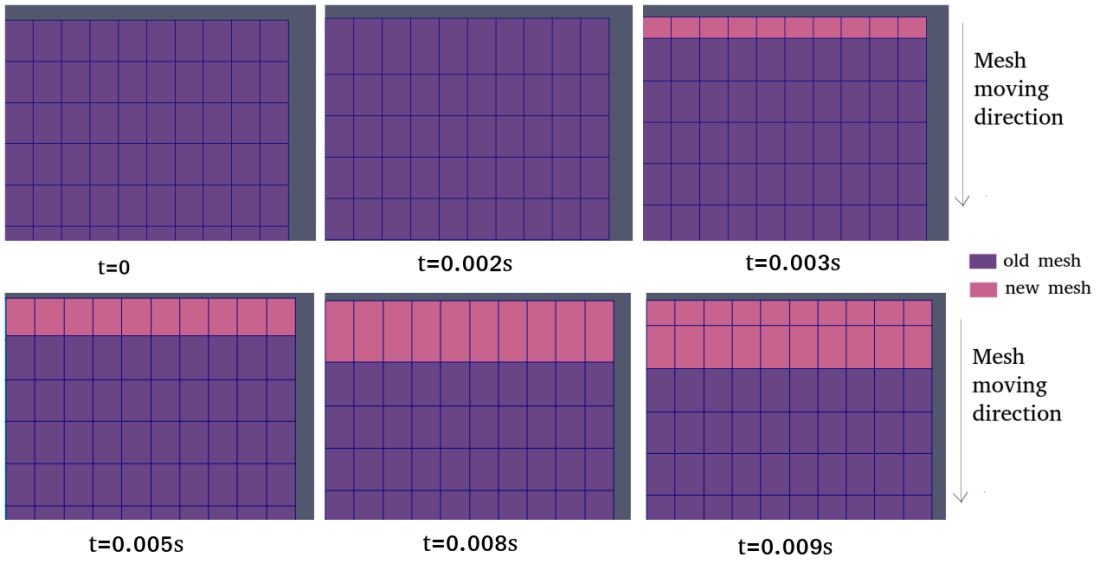

Figure 4.10: Layer addition/removal dynamic mesh algorithm - layer addition

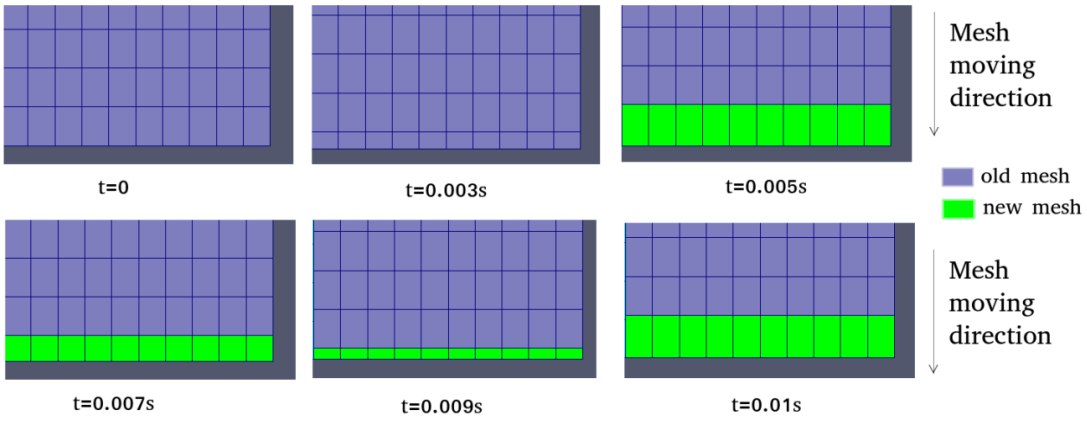

Figure 4.11: Layer addition/removal dynamic mesh algorithm - layer removal

Fig.4.10 shows when mesh is moving downward, new meshes (the pink meshes) will be added at the top of the computational domain. Fig.4.11 shows how meshes are removed when the mesh is moving downward and reaching the minimum threshold value.

Combination of AMI and A/R

The idea of combining AMI and A/R comes from tutorial *sphereDrop* in *OpenFOAM*(Greenshields, 2018). The mesh set up of this tutorial is shown in Fig.4.12. The left blue region is a steady mesh region separating the right A/R dynamic mesh region by AMI interface in between these two regions.

In this tutorial, the sphere is dropping downward by gravity. New meshes will be added at the top of the pink part if the mesh size is larger than the maximum threshold value. Old meshes will be removed at bottom of the purple part if mesh size is smaller than the threshold value. Once the topology changes of the mesh is done, old values in old mesh at old time step will be mapped to the new mesh at next time step.

By using combination of AMI and A/R, the mesh quality can stay constant in steady mesh region during calculation. The most concerned part during simulation

can be put in the steady mesh region to get a relatively accurate result.

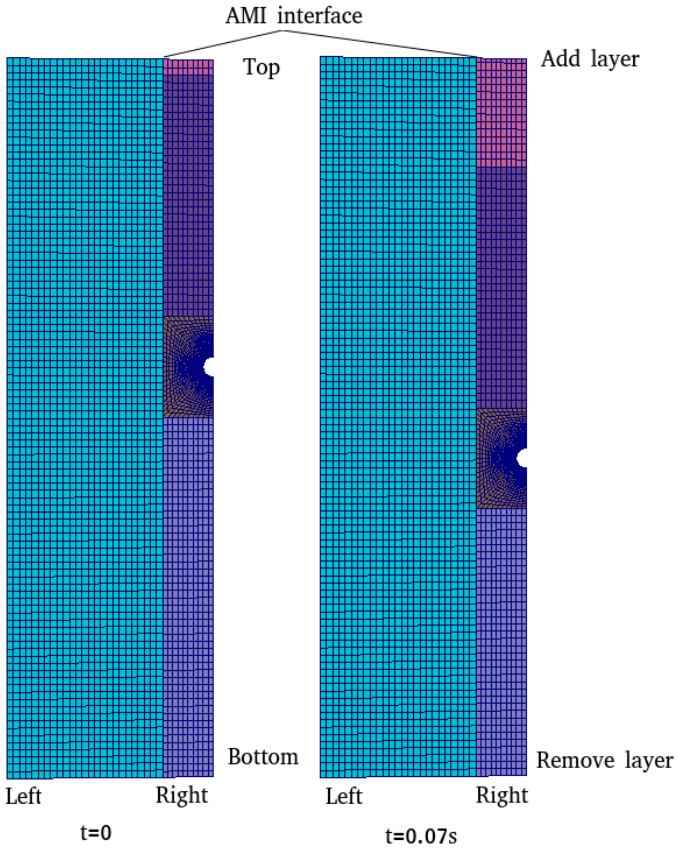

Figure 4.12: 2D sphere drop with both AMI and A/R dynamic mesh algorithm

Chapter 5

Numerical validation for dynamic mesh model

In this section, numerical validation will be done to check the feasibility of using dynamic mesh algorithms. The validation is done by comparing the results calculated from dynamic mesh with the results calculated from steady mesh. The use of dynamic mesh algorithm will bring errors e.g. mass loss or gain, interpolation error. In this section, test case lock-exchange will be done to check how large the error is.

The main difference between dynamic mesh and steady mesh is the motion of the mesh. In dynamic mesh algorithms, when mesh is moving, values from old mesh will be mapped to the new mesh. The faster the mesh is moving the more interpolation and mapping procedures will be done. Mapping and interpolation will introduce numerical error. Therefore, the mesh moving velocity can influence the numerical error during simulation.

Four different mesh moving velocities are tested in this section, which are 0.01, 0.02, 0.04 and 0.06 m/s. Four results of lock-exchange experiment will be used as validation data in the numerical experiment:

- Flow patterns difference

- *Froude* number $F_H = \frac{U}{\sqrt{g'h}}$, the dimensionless front speed of flow
- Total mass of the computational domain
- COG (center of gravity) of the fluids at certain time

To achieve the moving jet moving jet penetrating cohesive soil simulation, drift-flux model and dynamic mesh algorithms AMI and A/R are required. `driftFluxDyMFoam` is a drift-flux model solver with dynamic mesh algorithms developed by Gill (2016) for `OpenFOAM` version `v3.0.1`. Unfortunately, in `OpenFOAM` version `v3.0.1`, AMI and A/R dynamic mesh algorithms are not existing. In `OpenFOAM` version `v1812`, A/R and AMI are available to achieve the moving jet modeling. Therefore, a new drift-flux model plus dynamic mesh algorithms solver, `driftFluxDyMFoamv1812`, for `OpenFOAM` version `v1812` is built and applied for the moving jet penetrating cohesive soil simulation in this thesis. In this chapter, `driftFluxDyMFoamv1812`, is used to check the error of the dynamic mesh.

Two dynamic mesh algorithms have been chosen for modeling the moving jet, which are A/R (cell layer addition/removal) and AMI (arbitrary mesh interface). The modeling of the moving jet can be achieved by these two methods:

- Only using A/R dynamic mesh algorithm.
- Combine A/R and AMI dynamic mesh algorithms.

In the following sections, feasibility of these two dynamic mesh methods will be tested.

5.1 Lock-exchange physics

Before doing the simulation, the physics behind lock-exchange test will be introduced. In lock-exchange experiment, two different fluids with different densities will initially be separated by a vertical lock gate putting in the middle of them. The fluids are at rest before the lock gate is removed. After removing the lock

gate, the two fluids will start mixing. The denser fluid will flow along the bottom of the tank, while the lighter fluid will flow along the top of the tank. The motion of the flow is caused by the gravity and density difference of two fluids. The difference of the density is described by density ratio $\gamma = \rho_1/\rho_2$ (Shin et al., 2004). The density ρ_2 has a larger value than ρ_1. In this numerical experiment ρ_2 is 1000 kg/m^3, ρ_1 is 996 kg/m^3. The density ratio in this numerical experiment is $\rho_1/\rho_2 = 0.996$. This is a Boussinesq lock exchange case, because the density difference is small(Goeree et al., 2016). The kinetic viscosity of both fluids are the same, which is 1.004×10^{-6} m^2/s. The setup of the experiment is shown in Fig.5.1.

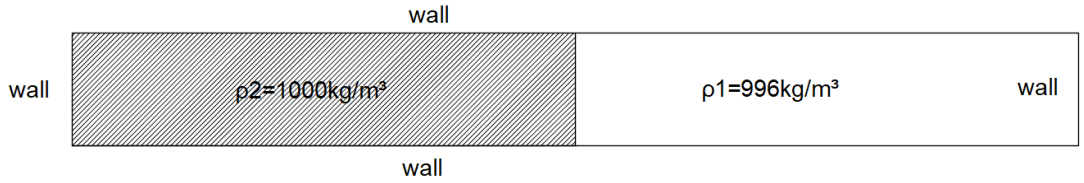

Figure 5.1: Experiment set up for lock-exchange test. The denser fluid is put to the left of the lock gate with $\rho_2 = 1000kg/m^3$ and the lighter fluid is put to the right of the lock gate with $\rho_1 = 996kg/m^3$. The lock gate is put in the middle of them. All fluids are sealed inside the surrounding wall.

5.2 Initial and boundary conditions

In this section, the initial and boundary conditions for numerical experiment will be introduced. The computational domain is shown in Fig.5.1. The length, width and height of the computational domain are L=1.8m, D=0.2m and H=0.2m separately. Uniform 2D Cartesian grids with a local length of 0.005m are used in the calculation.

The boundary conditions are shown in Fig.5.2. No slip wall boundary condition is used for velocity field on the walls. Zero gradient boundary condition is used for pressure on the walls. Zero gradient boundary condition is also applied for

concentration field on the walls.

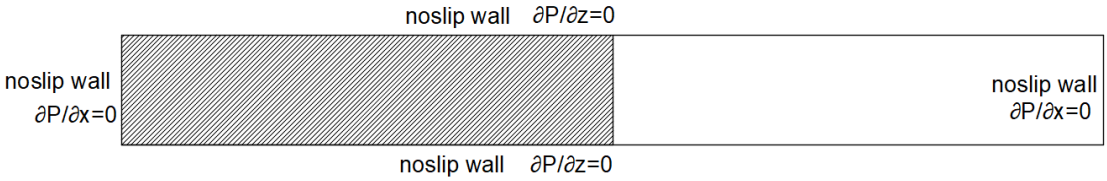

Figure 5.2: Boundary condition for lock-exchange test. No slip wall boundary condition for velocity field and zero gradient for pressure field

The initial conditions are shown in Fig.5.1. The initial concentration of the heavy and light fluid are 0.1 and 0 respectively. The densities are $\rho_1 = 996\ kg/m^3$ and $\rho_2 = 1000\ kg/m^3$. The time step in numerical calculations is adjustable corresponding to the *Courant* number.

The initial dynamic mesh set up for AMI combined A/R and only using A/R cases are shown in Fig.5.3 (a) and Fig.5.3 (b) separately. The blue mesh region in Fig.5.3 (b) is the steady mesh part, separating the dynamic mesh region above by AMI interface. The mesh will move to the right direction with a certain speed. Mesh profiles at 25 seconds are shown in Fig.5.4. Comparing Fig.5.3 and Fig.5.4, the mesh motion can be clearly seen.

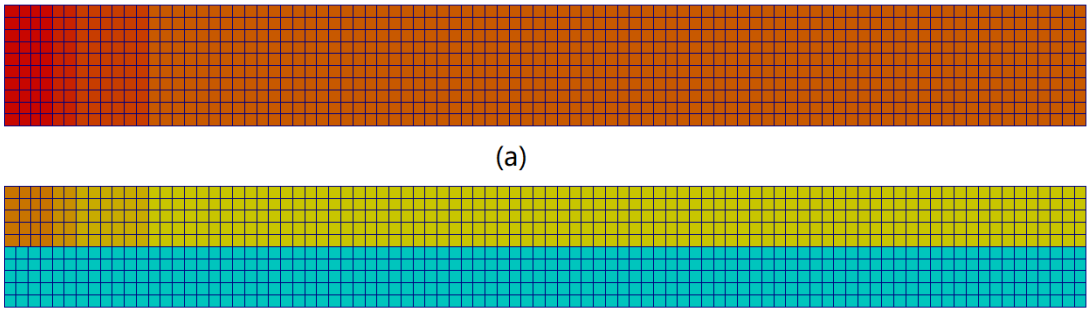

Figure 5.3: The above mesh set up is for only using A/R case. The below mesh set up is for AMI combined A/R case. Time = 0 sec, mesh moving velocity = 0.01m/s.

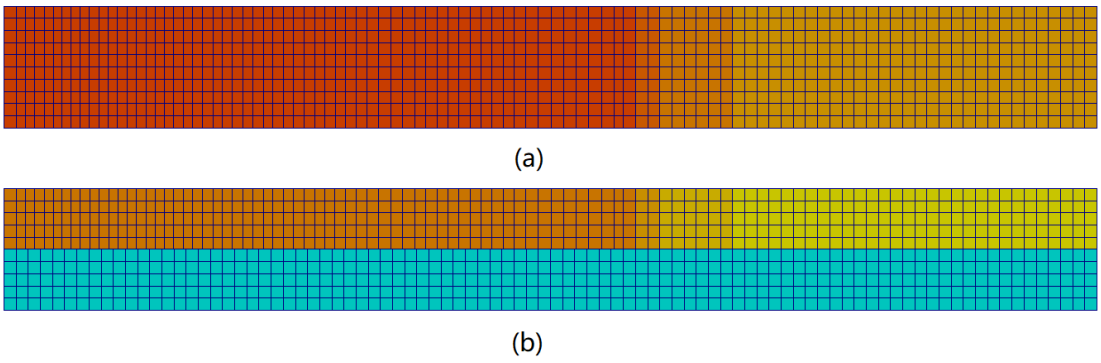

Figure 5.4: The above mesh set up is for only using A/R case. The below mesh set up is for AMI combined A/R case. Time = 25 sec, mesh moving velocity = 0.01m/s.

5.3 Results

In this section, results comparison between steady and dynamic mesh methods will be presented. The flow patterns, *Froude* number F_H, total mass of the fluid and the COG of the fluid will be used as references.

5.3.1 Flow patterns

In this section, the flow patterns of both dynamic mesh methods compared with steady mesh will be shown. The flow patterns of only using A/R and AMI combined A/R are shown in Fig.5.5 and Fig.5.6 separately.

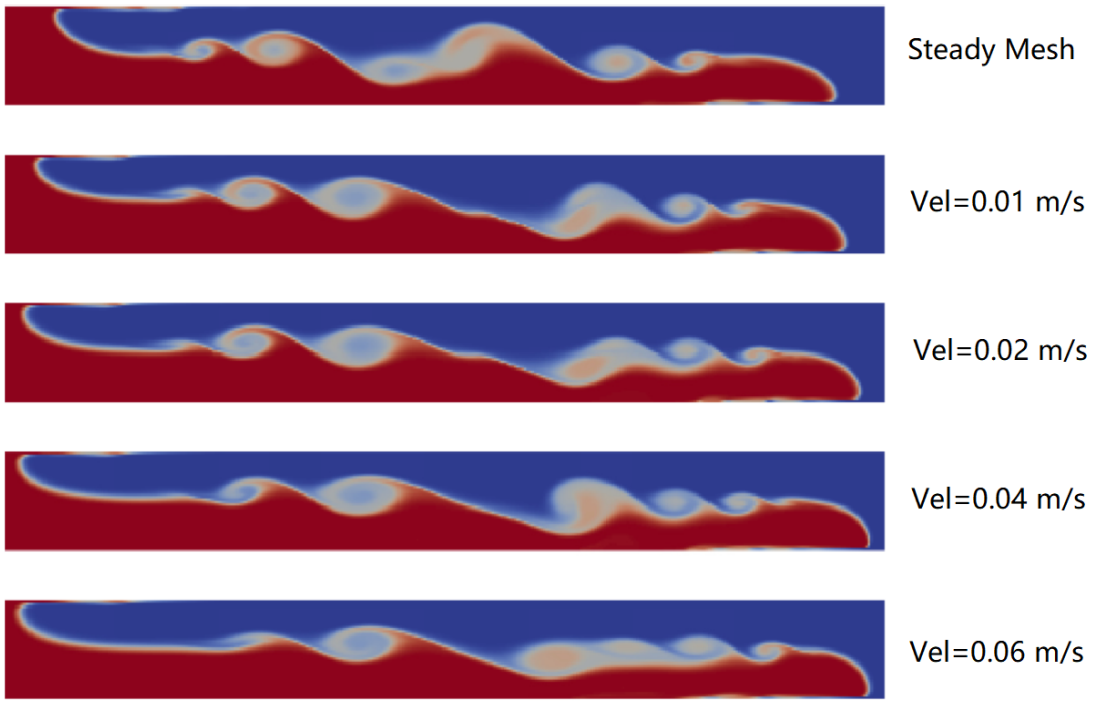

Figure 5.5: Flow pattern calculated by A/R dynamic mesh algorithm at 21 seconds. Mesh moving velocity: 0.01 m/s, 0.02 m/s, 0.04 m/s and 0.06 m/s

The results in Fig.5.5 and Fig.5.6 reveal that both dynamic mesh methods can bring errors. Compared the results calculated by using A/R dynamic mesh algorithm, AMI combined A/R has a lower error. The mixing waves pattern of AMI combined A/R looks relatively similar to the result of steady mesh. It can also be seen that the faster the mesh is moving, the larger the error will be.

In Fig.5.5, it can be seen that both light and heavy front of the density flow moves faster when A/R dynamic mesh algorithm is used. In Fig.5.6, it can be seen that only light front moves notably faster when AMI combined A/R is used. The reason is when AMI combined A/R dynamic mesh method is used, the heavy front of the density flow is staying in the steady mesh region while the light front of the density flow is staying in the dynamic mesh region. It means the exiting of steady mesh region can reduce the error. The most concerned part in the simulation can be then put in the steady mesh region to reduce error. This is an advantage of AMI combined A/R method over only using A/R method.

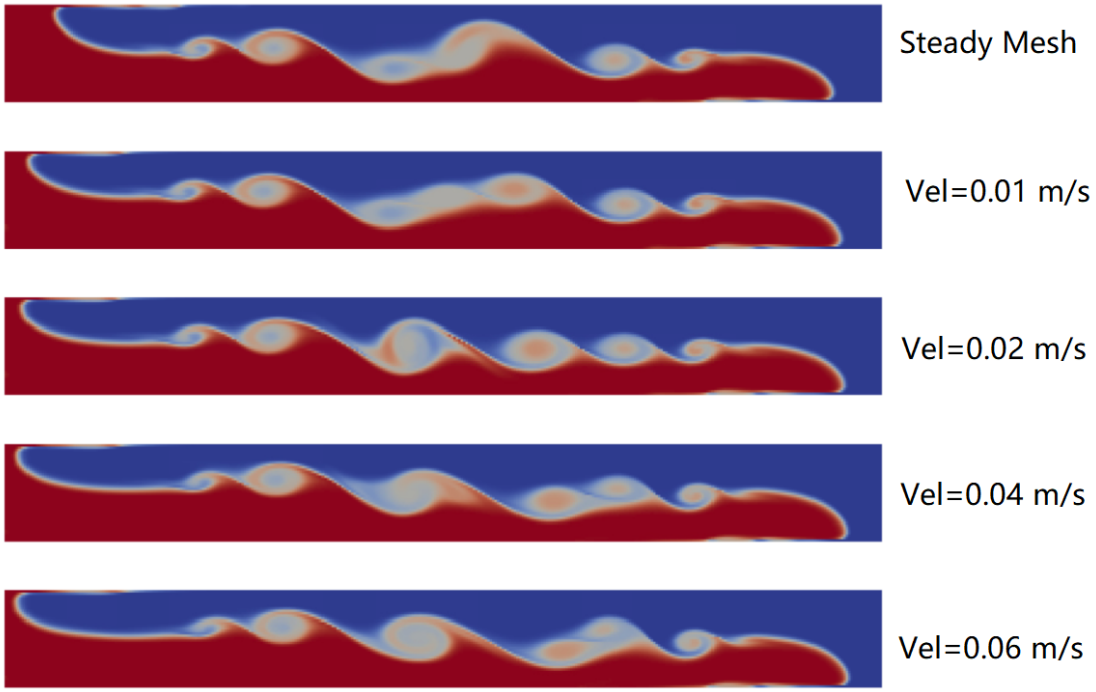

Figure 5.6: Flow pattern calculated by AMI + A/R dynamic mesh algorithm at 21 seconds. Mesh moving velocity: 0.01 m/s, 0.02 m/s, 0.04 m/s and 0.06 m/s

5.3.2 Dimensionless front speed *Froude* number F_H

In this section, the dimensionless front speed, *Froude* number $F_H = \frac{U}{\sqrt{g'h}}$, calculated from both steady mesh and dynamic mesh will be compared. In lock-exchange experiment, the *Froude* number is determined by the density difference of the two fluids, gravity acceleration g, height of the lock-gate H and the front speed U of the density current. It can be found that only the front speed U of the density current varies among different simulation cases. This means the difference of the *Froude* number F_H calculated from different cases is determined by the difference of the density current front speed U. The front speed U is calculated from the change rate of the density current front position. The density current front positions over time are shown in Fig.5.7.

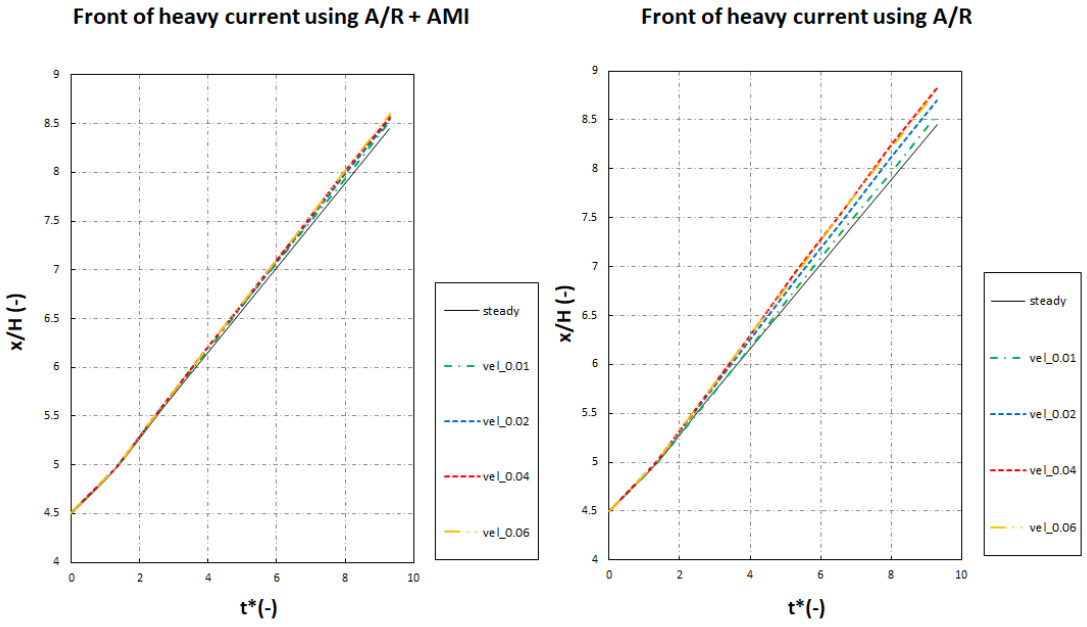

Figure 5.7: Dimensionless front position of density flow over time of numerical lock-exchange experiment

Seen from Fig.5.7, the front positions of the density current are linearly increasing with respect to time. This means the front speed of the density current is constant, which agrees with Shin et al. (2004). By calculating the slope of the lines, the

front speed U of the density currents are known. The *Froude* number can then be calculated by $F_H = \frac{U}{\sqrt{g'h}}$ using the velocity U calculated from the slope in Fig.5.7.

The *Froude* number F_H of both heavy and light currents calculated by `driftFluxDyMFoam1812` are shown in Table.5.1 and Table.5.2 below. The errors in the table are calculated as $err = |\frac{F_{Hd}-F_{Hs}}{F_{Hs}}|$, where F_{Hd} is the *Froude* number of dynamic mesh cases. F_{Hs} is the *Froude* number of steady mesh case.

Table 5.1: Heavy density current F_H error comparison among different mesh moving speed

`driftFluxDyMFoamv1812` with AMI and A/R dynamic mesh

	steady	vel_0.01	vel_0.02	vel_0.04	vel_0.06
F_H	0.433	0.439	0.445	0.445	0.452
Err F_H		1.45%	2.90%	2.90%	4.35%

`driftFluxDyMFoamv1812` with A/R dynamic mesh

	steady	vel_0.01	vel_0.02	vel_0.04	vel_0.06
F_H	0.433	0.445	0.458	0.470	0.470
Err F_H		2.90%	5.80%	8.70%	8.70%

Table 5.2: Light density current F_H error comparison among different mesh moving speed

`driftFluxDyMFoamv1812` with AMI and A/R dynamic mesh

	steady	vel_0.01	vel_0.02	vel_0.04	vel_0.06
F_H	0.433	0.461	0.467	0.470	0.476
Err F_H		6.52%	7.83%	8.70%	10.00%

`driftFluxDyMFoamv1812` with A/R dynamic mesh

	steady	vel_0.01	vel_0.02	vel_0.04	vel_0.06
F_H	0.433	0.452	0.467	0.470	0.467
Err F_H		4.35%	7.83%	8.70%	7.83%

Comparing the error of F_H among heavy current cases in Table.5.1, using AMI combined A/R dynamic mesh method has lower error than only using A/R dynamic mesh algorithm. By using AMI combined A/R dynamic mesh method, the heavy flow can stay at the steady mesh region, where mesh quality is constant. Because of this, the error of AMI combined A/R cases can be smaller.

Comparing the error of F_H through the light current cases in Table.5.2, both dynamic mesh methods have a relatively larger error. The reason is the front of light density current for both dynamic mesh methods stay at dynamic mesh region during calculation. Besides, the faster the mesh is moving the larger the error is.

By comparing the F_H error for both dynamic mesh methods, it can be found that when doing the calculation, the most concerned area can be placed in the steady mesh region to reduce error. And this is the advantage of AMI combined A/R dynamic mesh algorithm over only using A/R dynamic mesh algorithm.

5.3.3 COG comparison and mass conservation check

Using dynamic mesh can also influence the COG of the currents and bring mass conservation error. In this section, both COG position and mass conservation will be checked. The mass conservation and COG position are checked at $t = 21s$.

First, the mass conservation is checked. The results are shown in Table.5.3. It can be seen that the mass conservation can be ensured. The error between the steady mesh case and all dynamic mesh cases are around 0.001%.

The COG positions at $t = 21s$ are shown in Table.5.4. Both x and z coordinates of the COG are checked. The COG is calculated by Eq.(5.1) and Eq.(5.2).

$$COG_x = \frac{\Sigma c_i \rho x}{\Sigma c_i \rho} \tag{5.1}$$

$$COG_z = \frac{\Sigma c_i \rho z}{\Sigma c_i \rho} \tag{5.2}$$

where c_i is the concentration of phase i. The results in Table.5.4 shows that the errors are within 10%. The faster the mesh moves, the larger the error is. It can also be seen that A/R brings more error than combining AMI and A/R.

Table 5.3: Mass conservation check at 21 seconds

`driftFluxDyMFoamv1812` with AMI and A/R dynamic mesh

	steady	vel_0.01	vel_0.02	vel_0.04	vel_0.06
Mass	3.60000	3.59991	3.59994	3.59989	3.59995
Mass_err		0.002%	0.002%	0.003%	0.001%

`driftFluxDyMFoamv1812` with A/R dynamic mesh

	steady	vel_0.01	vel_0.02	vel_0.04	vel_0.06
Mass	3.60000	3.60002	3.60002	3.60000	3.59997
Mass_err		0.001%	0.001%	0.000%	0.001%

Table 5.4: COG position check at 21 seconds

`driftFluxDyMFoamv1812` with AMI and A/R dynamic mesh

	steady	vel_0.01	vel_0.02	vel_0.04	vel_0.06
COG_x	0.744	0.768	0.768	0.773	0.778
Err_COG_x		3.31%	3.32%	4.03%	4.59%
COG_z	0.0613	0.0589	0.0587	0.0584	0.0583
Err_COG_z		3.85%	4.23%	4.70%	4.94%

`driftFluxDyMFoamv1812` with A/R dynamic mesh

	steady	vel_0.01	vel_0.02	vel_0.04	vel_0.06
COG_x	0.744	0.745	0.777	0.798	0.803
Err_COG_x		0.23%	4.45%	7.30%	8.05%
COG_z	0.0613	0.0598	0.0578	0.0571	0.0564
Err_COG_z		2.51%	5.71%	6.94%	8.01%

5.4 Summary and remarks

In this section, two dynamic mesh methods, only using A/R and AMI combined A/R, have been validated with the steady mesh result by a lock-exchange numerical experiment. Flow patterns, *Froude* number F_H, COG position and mass conservation are used as the validation reference.

From the results of both dynamic mesh methods, it can be concluded that the faster the mesh moves, the larger the error is. The reason is when the mesh moves faster, more interpolation and mapping will happen. These procedures will bring numerical error.

The mass conservation check shows that both dynamic mesh methods introduce no mass gain or loss. But when comparing the flow pattern, F_H and COG of both dynamic mesh methods, AMI combined A/R shows advantage over only using A/R. The error of these references calculated from AMI combined A/R method

are all smaller than only using A/R. Due to the comparison above, the suggestions for modeling the moving jet in this thesis will be using AMI combined A/R method instead of only using A/R method.

Chapter 6

CFD modeling of moving jet penetrating cohesive soil

In this chapter, the moving jet CFD simulation will be done. The drift-flux model and dynamic mesh AMI and A/R introduced in Chapter 3.3 and Chapter 4.4 will be used. Solver `driftFluxDyMFoamv1812` made by the author will be used for calculation. In Section 6.1, the mesh setup, initial conditions and boundary conditions will be explained. In Section 6.2, the results of the CFD numerical simulation will be validated with experimental results from Nobel (2013). The validated results are:

- The failure modes of soil during jetting
- The dimensionless soil cavity depth Z_c/D_n at different jet traverse velocity v_t when jet ratio $p_j/su = 19.5$
- The clay surface dislodgement rate during jetting

6.1 Numerical setup

In this section, the numerical setup for simulation will be introduced. In Section 6.1.1, the mesh setup will be shown. In Section 6.1.2 and 6.1.3, the initial and boundary conditions will be described.

6.1.1 Mesh setup and mesh sensitivity check

To model the moving jet, dynamic mesh methods are used in this thesis. In Chapter 5, it is found that AMI combined A/R has advantage over only using A/R. In this thesis combination of AMI and A/R will be used modeling the moving jet penetrating clay process.

By combining AMI and A/R dynamic mesh algorithm, the moving jet can be put in the A/R dynamic mesh region, while the soil can be placed in the steady mesh region. The steady mesh region and A/R dynamic mesh region are separated by AMI interface. By putting the soil in the steady mesh region, the soil failure process can be calculated more accurately. The setup of the dynamic mesh regions at $t = 0$ is shown in Fig.6.1. After one second, with a mesh moving velocity of $v_{mesh} = 1.5m/s$, the mesh region layout becomes what is shown in Fig.6.2.

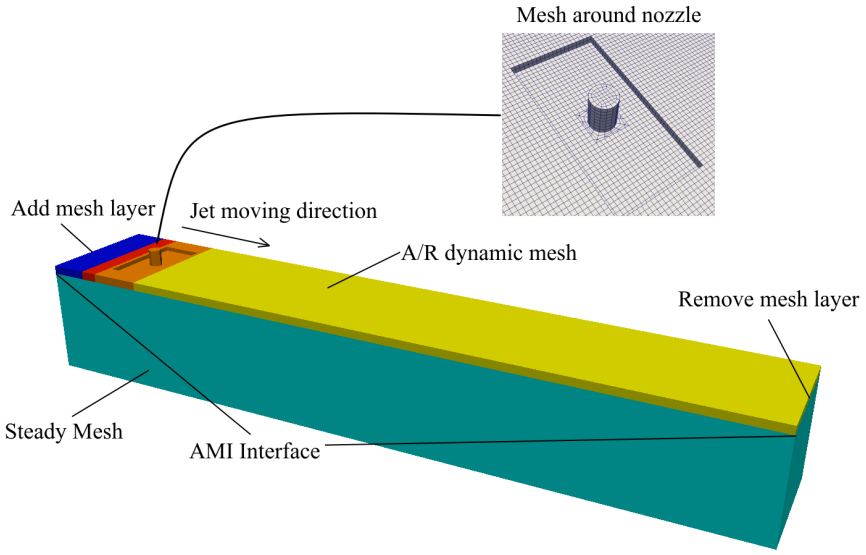

Figure 6.1: Mesh region layout of moving jet penetrating cohesive soil clay using AMI and A/R at $t = 0s$, mesh moving velocity $v_{mesh} = 1.5m/s$

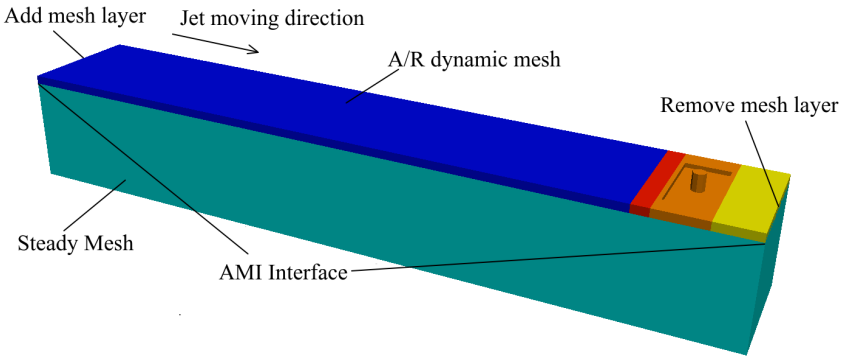

Figure 6.2: Mesh region layout of moving jet penetrating cohesive soil clay using AMI and A/R at $t = 1s$, mesh moving velocity $v_{mesh} = 1.5m/s$

The bottom green part is the steady mesh region, separating the A/R dynamic mesh region by the AMI interface. When the jet is moving from left to right, new cells are added to the left and old cells are removed from the right.

Table 6.1: Mesh sensitivity check: dimensionless soil cavity depth at different jet traverse velocity of two mesh sizes($0.01m$ and $0.005m$)

V_t (m/s)	Z_c/D_n $(mesh0.01)$	Z_c/D_n $(mesh0.005)$	error
0.25	5.33	5.27	1.27%
0.50	4.67	4.65	0.43%
1.00	4.00	3.83	4.35%
1.49	3.67	3.57	2.80%
1.83	3.50	3.48	0.59%

Two mesh sizes, $0.01m$ and $0.005m$, have been used for calculation. As the limitation of the computational power, the smallest mesh size is limited to $0.005m$. A mesh convergence check is carried out by comparing the soil dimensionless cavity depth at different traverse velocity. The results are shown in Fig.6.3 and Table.6.1. Even though a finer mesh cannot be used for simulation as the limitation of computational power, the error between two mesh size is within 5%. If more computational power is available in the future, calculations with finer mesh can be conducted to check the sensitivity of the mesh more accurately.

In Fig.6.3 and Table.6.1, it can be found that the error is not constant at different jet traverse velocity. When jet traverse velocity increases, soil failure modes will change from penetrating jet to deflecting jet. Compared with finer mesh cases, some of the soil failure mechanisms cannot be captured during the simulation in coarse mesh cases. Therefore, during the transition from penetrating jet to deflecting jet, the error increases to 4.35% when jet traverse velocity is $1m/s$.

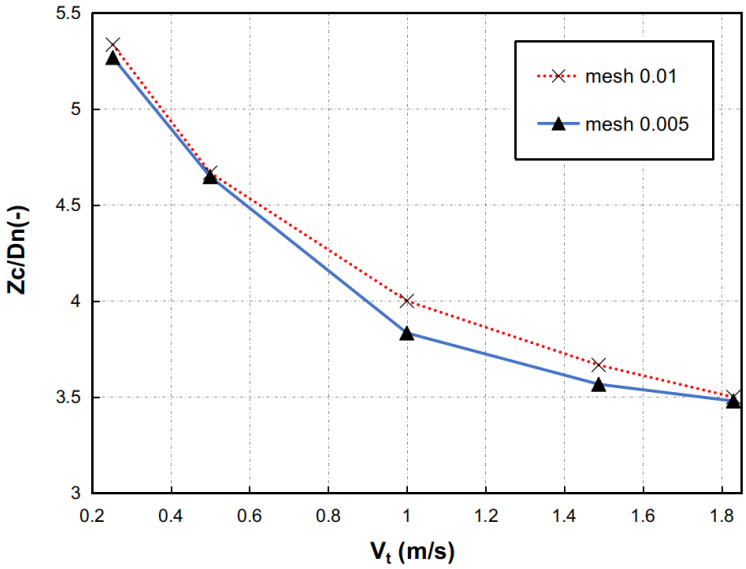

Figure 6.3: Mesh sensitivity check: dimensionless soil cavity depth comparison at different jet traverse velocity of two mesh sizes ($0.01m$ and $0.005m$).

6.1.2 Initial conditions setup

The soils are put in the steady mesh region as mentioned in Section 6.1.1. Fig.6.4 shows the initial condition of the concentration field. The red part stands for the soils while the blue part represents water. The volume concentration of the soils are quantified by α_s (volume concentration of soil) in `driftFluxDyMFoamv1812` solver. The initial volume concentration of the soil is 0.576 referring to Nobel (2013) for validation. The blue part, which represents water, has a zero value of *alpha.sludge*.

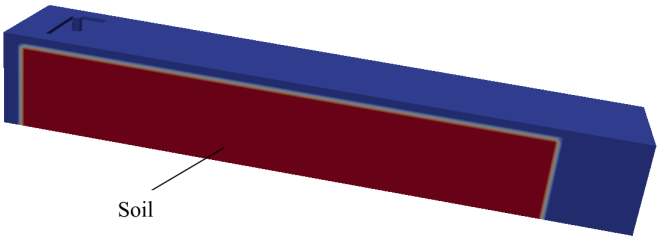

Figure 6.4: α_s layout in whole computational domain in 3D

The soil used here is the cohesive soil clay. The clay has a yield stress of 23 KN/m^2 and density of 2588 Kg/m^3. To validate the result with the work of Nobel (2013), the jet inlet velocity is set as 30 m/s w.r.t jet pressure $p_j = 0.45Mpa$. Therefore, the jet ratio $p_j/su = 19.5$, which is the same as the work of Nobel (2013). The initial concentration field of the soil is shown in Fig.6.5.

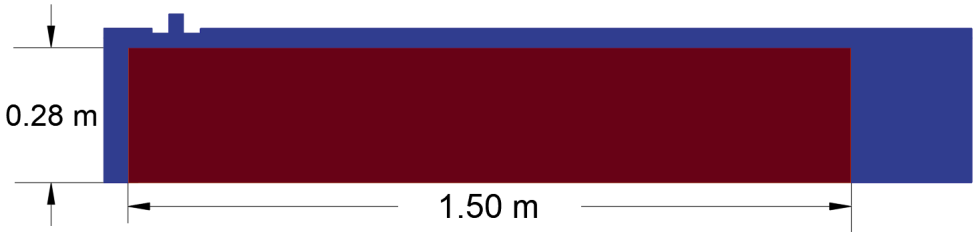

Figure 6.5: Side view of initial concentration field : the clay has a 1.5 m length, 0.15 m width(not shown in this figure), 0.28 m depth. The blue part is water, the red part is clay. The length, width and height of the computational domain are $1.8m$, $0.15m$ and $0.3m$.

The jet in Fig.6.5 is a round jet with a diameter of 30 mm. The SOD (stand off distance: distance between jet outlet and soil surface) is 20 mm, which is the same as the setup mentioned in thesis of Nobel (2013).

6.1.3 Boundary conditions setup

Fig.6.7 and Fig.6.8 show the side view and front view of the computational domain with boundary conditions setup. The clay is placed in between the two side walls. Outlet boundary conditions are implemented in front, end and top of the computational domain. No slip boundary condition is applied to the walls. Dirichlet boundary condition is implemented to the jet inlet. Wall functions (Wilcox et al., 1998) are applied to the turbulence dissipation rate ϵ and turbulence kinetic energy k on the walls. The description of wall functions refers to section 3.4.2. The initial value of k and ϵ need estimations, which follow Eq.(3.32) and Eq.(3.33). Table.6.2 shows the detailed boundary conditions setup of the computational domain. It has to be mentioned that no boundary condition is applied to the interface between water and soil. In this numerical model, the concentration at the soil water interface is not changing sharply but gradually, see Fig.6.6. The reason is the soil at the soil water interface is not only cut but also fluidized by the jet flow. The fludized soil has a volume concentration in between the water and the unfluidized soil. Therefore, the soil volume concentration profile at the soil water interface is assumed to change gradually, but not sharply.

Table 6.2: Boundary conditions set up at different positions for all variables

	$U\ (m/s)$	$p_{rgh}\ (pa)$	$k\ (m^2s^{-2})$	$\epsilon\ (m^2s^{-3})$	$\alpha_s\ (-)$
walls	noSlip	zeroGradient	WallFunction	WallFunction	zeroGradient
outlet	zeroGradient	Dirichlet	inletOutlet	inletOutlet	inletOutlet
inlet	Dirichlet	zeroGradient	Dirichlet	Dirichlet	Dirichlet

Note: U is the velocity. $P_{rgh} = P - \rho gh$, which is the pressure without hydro-static pressure. k is the turbulence kinetic energy, ϵ is the turbulence dissipation rate. α_s is the soil volume concentration.

The dynamic mesh algorithm also needs a boundary condition setup. The motion of the mesh is controlled by file `pointDisplacement` in *OpenFOAM*. The walls, which do not move during simulation, has a zero fixed value of displacement boundary condition. The jet, which has a constant moving velocity, is defined as boundary condition type *solidBodyMotionDisplacement* with a certain moving velocity in *OpenFOAM*.

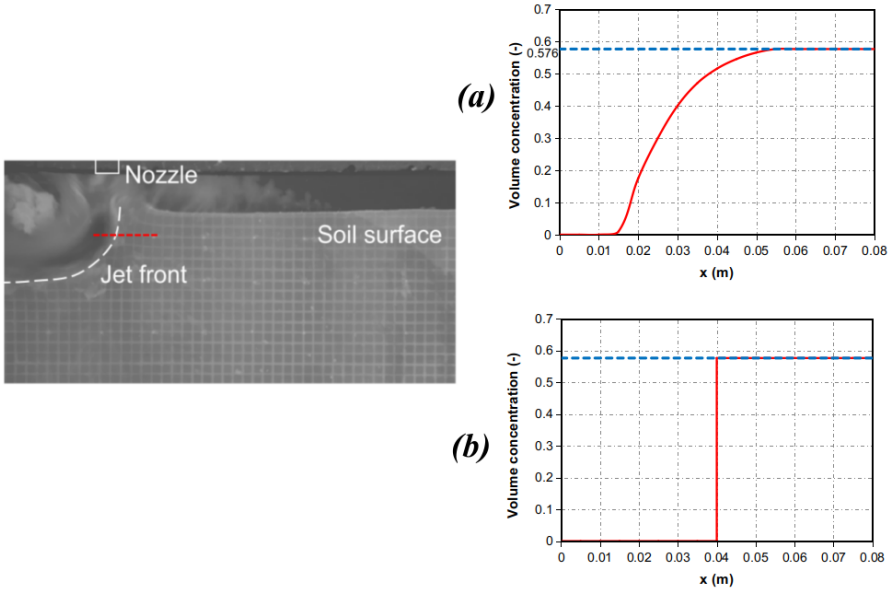

Figure 6.6: The soil volume concentration profile along the red dash line in the left figure is assumed to follow the volume concentration changing rule of figure(a). In figure(a), the volume concentration of soil at the soil water interface increases gradually, while that in figure(b) changes sharply.

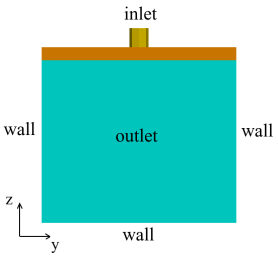

Figure 6.7: Boundary conditions setup side view

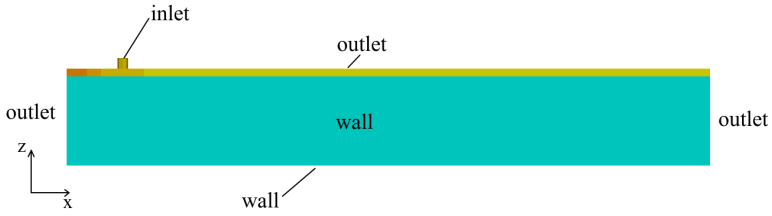

Figure 6.8: Boundary conditions setup front view

6.2 Comparison with experiment

In this section, numerical results of moving jet penetrating cohesive soil clay will be validated with work of Nobel (2013). The mesh sensitivity check has been carried out in section 6.1.1. The residual convergence is also ensured before doing the simulation. For example, the residual convergence of the case when jet ratio is $p_j/su = 19.5$ and jet traverse velocity $v_t = 1.83m/s$ is shown in Fig.6.9. In Fig.6.9, the final residual after iterations at each time step is shown. It can be seen that the residual of each variable is controlled under its residual tolerance.

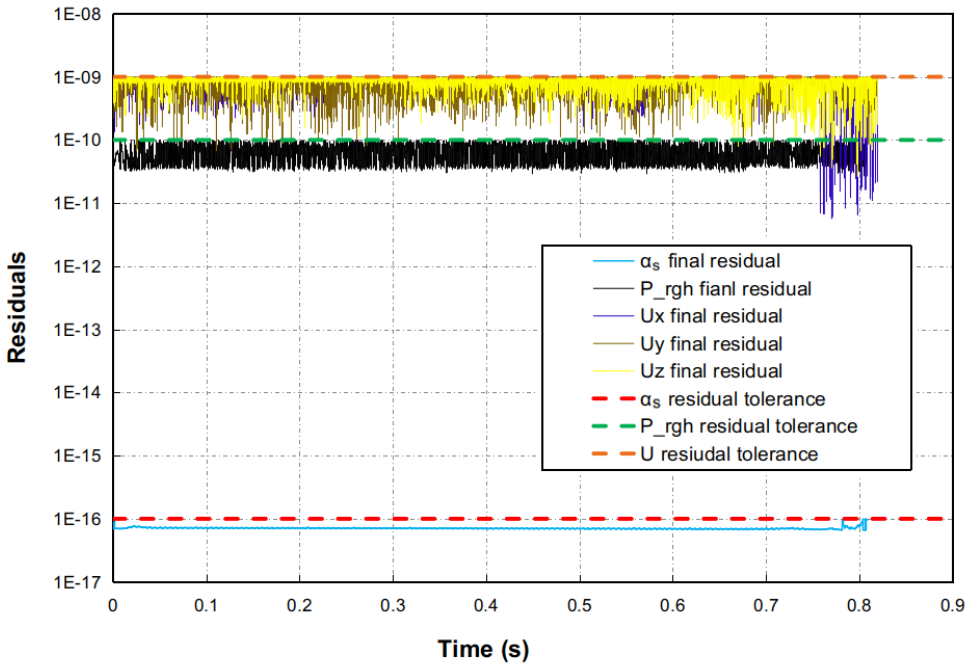

Figure 6.9: Residual convergence check of the case when jet ratio is $p_j/su = 19.5$ and jet traverse velocity $v_t = 1.83m/s$. Residual convergence of soil volume concentration α_s, pressure P_{rgh} and velocity in three directions U_x, U_y and U_z are checked. The residual tolerance of α_s, P_{rgh} and U are 10^{-16}, 10^{-10} and 10^{-9} respectively.

6.2.1 Failure modes during jetting

As mentioned in Chapter 2, there are four failure modes during jetting. In this thesis, two modes, which are penetrating jet and deflecting jet are reproduced by CFD simulation. The results are shown in Fig.6.10.

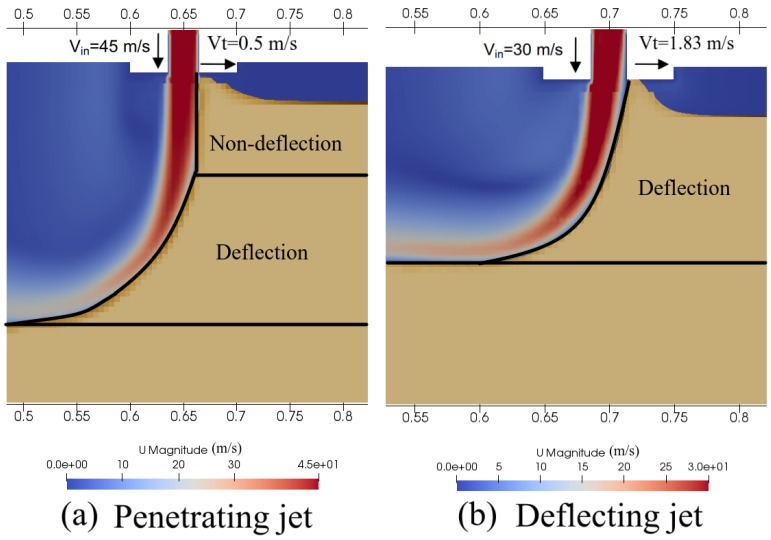

Figure 6.10: Failure modes calculated from CFD. Figure (a) represents the penetrating jet, with jet inlet velocity $V_{in} = 45m/s$, jet ratio $p_j/su = 38$ and jet traverse velocity $V_t = 0.5m/s$. Figure (b) represents the deflecting jet with jet inlet velocity $V_{in} = 30m/s$, jet ratio $p_j/su = 19.5$ and jet traverse velocity $V_t = 1.83m/s$. The brown parts represent soils, while the red parts represents jet flow.

The figure (a) in Fig.6.10 shows the case when jet traverse velocity is 0.5 m/s and jet ratio is $p_j/su = 38$. The figure (b) in Fig.6.10 shows the case when jet traverse velocity is 1.83 m/s and jet ratio is $p_j/su = 19.5$. It can be clearly seen that figure (a), which has two zones (non-deflection zone and deflection zone) can represent the penetrating jet. Figure (b), which has one zone (deflection zone) can represent the deflecting jet. This means both penetrating jet and deflecting jet mentioned in the work of Nobel (2013) can be reproduced by the CFD numerical model.

6.2.2 Dimensionless soil cavity depth at different traverse velocity with a jet ratio 19.5

In thesis of Nobel (2013), the cavity depth of the soil Z_c is nondimensionalized by the nozzle diameter D_n. The dimensionless soil cavity depth is calculated as Z_c/D_n. Jet ratio $p_j/su = 19.5$ with different jet traverse velocity v_t cases have been done in his experimental work. CFD calculations with same setup have been done in this thesis work to validate the CFD model. Fig.6.11 shows the comparison between CFD and experiment. The uncertainty of the experiment mentioned in Nobel (2013) is 20%, which is shown by the red uncertainty bar in Fig.6.11. Several remarks can be summarized from Fig.6.11:

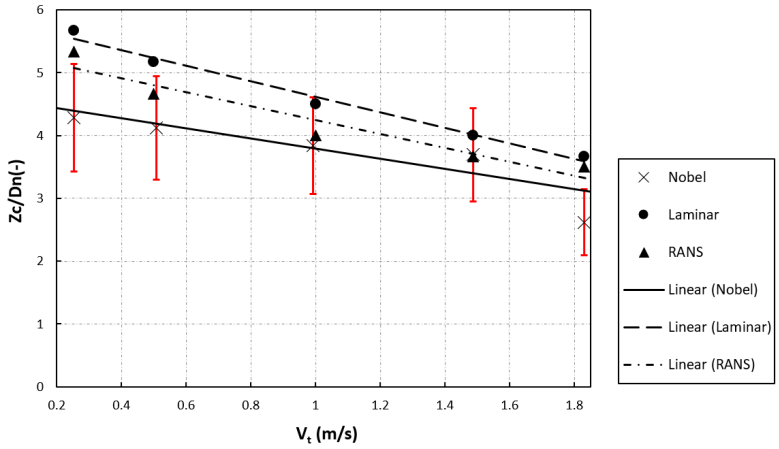

Figure 6.11: Dimensionless soil cavity depth at different jet traverse velocity when jet ratio $p_j/su = 19.5$. The uncertainty of experimental work is 20%, see red uncertainty bar. The dots represent the results calculated by laminar solver. The triangles represent the results calculated by $buoyant - k - \epsilon$ RANS model. The cross symbols represent experimental result from Nobel (2013). The dash lines are the linear trend lines of results calculated using laminar and RANS solver. The solid line is the linear trend line of experimental results(Nobel, 2013).

- Compared with laminar model, results calculated by $buoyant - k - \epsilon$ is closer to the experimental results of Nobel (2013).

- Both CFD models and experimental work show a decreasing trend of soil cavity depth as the jet traverse velocity increases.
- The trend lines are almost parallel to each other, meaning the slope of the trend lines are close to each other.

As the implementation of the $buoyant - k - \epsilon$ turbulence model, the energy dissipation due to the turbulence of the jet flow is considered. Therefore, the soil cavity depths calculated by using laminar model are deeper than using $buoyant - k - \epsilon$ model. As the increase of the jet traverse velocity, the time scale of the jet flow cutting cohesive soil process becomes shorter. As a result, the soil cavity depth becomes shallower as the the jet traverse velocity increases.

6.2.3 Clay surface dislodgement rate

In this section, the soil surface dislodgement rate calculated from CFD simulation will be compared with experimental results of Nobel (2013). The case with jet traverse velocity 0.5 m/s and jet ratio 38, which is a penetrating jet case, is used here for validation. Fig.6.12 shows the amount of soil dislodged during experiment. Seen from Fig.6.12, around 6 cells are removed after 0.003 sec jetting process. The size of the cells in Fig.6.12 is 6.25 $mm \times 6.25$ mm. Because of the limitation of the experimental data on hand, the transient soil surface dislodgement rate of the experiment cannot be calculated. With the experimental data on hand, the clay dislodgement rate is calculated as 0.078 m^2/s.

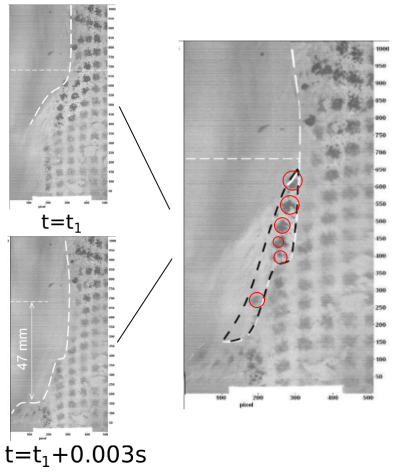

Figure 6.12: The amount of clay removed after $0.003s$ jetting from experiment(Nobel, 2013). From the figure, around 6 cells are removed after jetting. The jet traverse velocity is $v_t = 0.5\ m/s$ and jet ratio is $p_j/su = 38$.

The surface dislodgement rate of clay as a function of time calculated by CFD simulation is shown in Fig.6.13. The green dash line in Fig.6.13 represents the soil surface dislodgement rate of the experiment, which is 0.078 mm^2/s. From Fig.6.13, it can be found that the soil surface dislodgement rate of the experiment is in between the maximum and minimum value calculated by CFD model. It can also be seen that the soil surface dislodgement rate calculated by CFD model has a periodic behavior. The period of the soil surface dislodgement rate is equal to $0.02s$, see Fig.6.13.

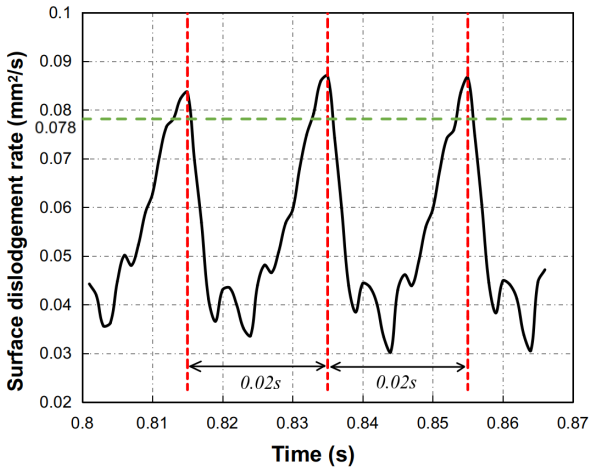

Figure 6.13: The soil surface dislodgement rate as a function of time calculated by CFD model. The green dash line represents the soil surface dislodgement rate of experiment, which is equal to 0.078 mm^2/s.

Chapter 7

Analysis based on CFD simulation

In this chapter, analysis based on this CFD model, which was not conducted by the experiment of Nobel (2013) will be carried out. The following objectives will be analyzed in this section:

- Soil volume dislodgement rate with respect to jet traverse velocity
- Pressure exerting on soil as a function of time
- Shear plane change during jetting as a function of time
- Jet inclination angle and deflection distance

7.1 Soil volume dislodgement rate with respect to jet traverse velocity

The volume dislodgement rate of soil during jetting w.r.t jet traverse velocity for a single moving jet will be discussed in this section. The volume change of soil

after jetting can be simulated by this CFD model, see Fig.7.1. The soil volume dislodgement rate $\dot{V_d}$ of soil is calculated as:

$$\dot{V_d} = V_d/T_d \tag{7.1}$$

where V_d is the dislodgement volume of soil, T_d is the time interval.

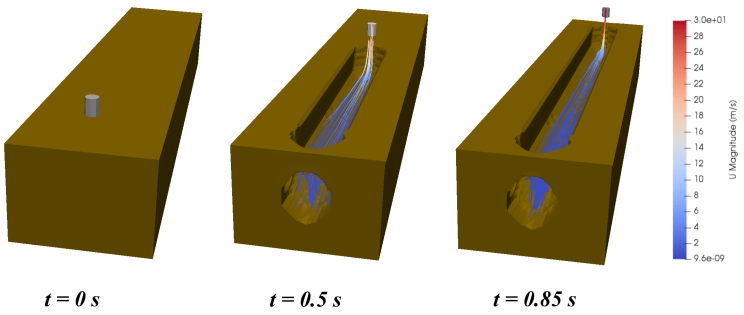

Figure 7.1: The soil concentration contour change as a function of time. The jet ratio is $p_j/su = 19.5$ and the jet traverse velocity is $v_t = 1.83m/s$.

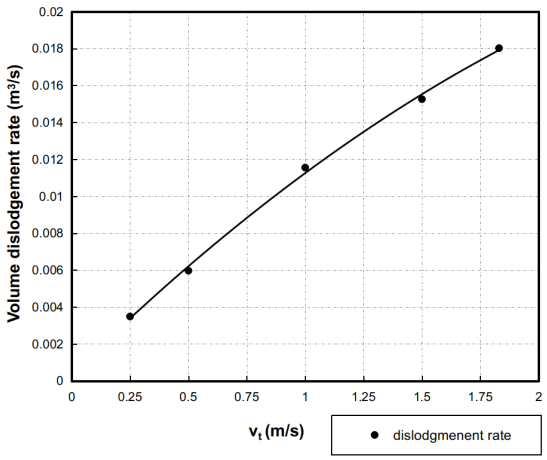

Figure 7.2: Soil dislodgement rate with respect to jet traverse velocity v_t. The jet ratio is $p_j/su = 19.5$.

The volume dislodgement rate of soil w.r.t jet traverse velocity for a single moving jet when jet ratio is $p_j/su = 19.5$ is shown in Fig.7.2. It can be found that when

jet traverse velocity is lower than $1.83m/s$, the volume dislodgement rate of soil increases as the jet traverse velocity increases. It means that for a single moving jet case, the increase of jet traverse velocity can bring a high volume dislodgement rate of soil. Higher jet traverse velocities are not studied in this thesis, due to the highest operation velocity of a dredging ship is usually lower than 2 knots ($\approx 1m/s$).

7.2 Pressure on soil surface over time

The cohesive soil fails when the pressure exerting on it is over the shear strength. The pressure is assumed to build up on the soil surface over time until the pressure exerting on the soil is large enough to break the soil. In experiment, the pressure on the soil is hard to detect. But CFD software can save the pressure profile as a function of time. Fig.7.3 shows the pressure profile of a point on the soil surface over time. It can be seen the pressure is building up on the soil surface when the jet flow is upon the soil surface. When the pressure is large enough to break the soil, the soil will be cut off and the pressure will decrease. When the jetting process is over, the pressure at the chosen position will decrease.

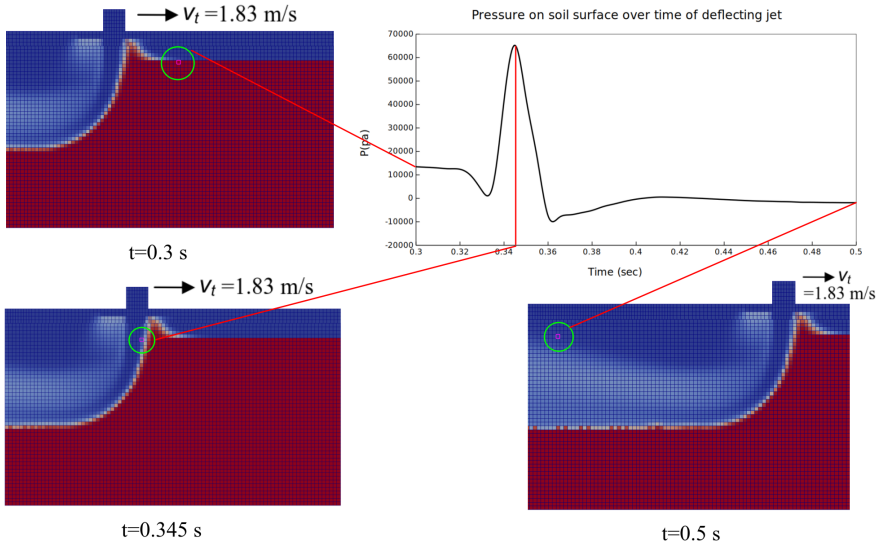

Figure 7.3: Pressure profile on soil surface of deflecting jet over time

7.3 Shear plane change as a function of time

The shear plane determines where the cohesive soil breaks during jetting. The real position of the shear plane is hard to determine. The shear plane in this thesis is determined by the second invariant I_2 of shear rate. When the shear rate is larger than zero, it means the soil is starting to flow.

Fig.7.4 and Fig.7.5 show the shear plane patterns of deflecting jet and penetrating jet over time. The deflecting jet has a traverse velocity $v_t = 1.83\ m/s$ and jet ratio $p_j/su = 19.5$. The penetrating jet has a traverse velocity $v_t = 0.5\ m/s$ and jet ratio $p_j/su = 38$. The shear plane pattern can be recognized by the colour difference shown in Fig.7.4 and Fig.7.5.

It can be found that the changing rule of shear plane pattern over time for deflecting jet and penetrating jet are different. The shear plane pattern of a deflecting jet is not changing over time, see Fig.7.4. But the shear plane pattern of penetrating jet has a periodic behavior as a function of time, see Fig.7.5.

In Fig.7.4, it can be found that the shear plane pattern of deflecting jet, which has a maximum radius of 90 mm, is not changing over time. In Fig.7.5, it can be seen the shear plane in the non-deflection zone of the penetrating jet is changing over time with a period of 0.02 s. The maximum radius of the shear plane of the penetrating jet is around 75 mm.

It can be concluded from the CFD results that the shear plane pattern change is determined by the failure mode during jetting. The shear plane pattern is not changing for deflecting jet, which only has a deflection zone. For a penetrating jet, which has both non-deflection zone and deflection zone, the shear plane pattern has a periodic behavior over time.

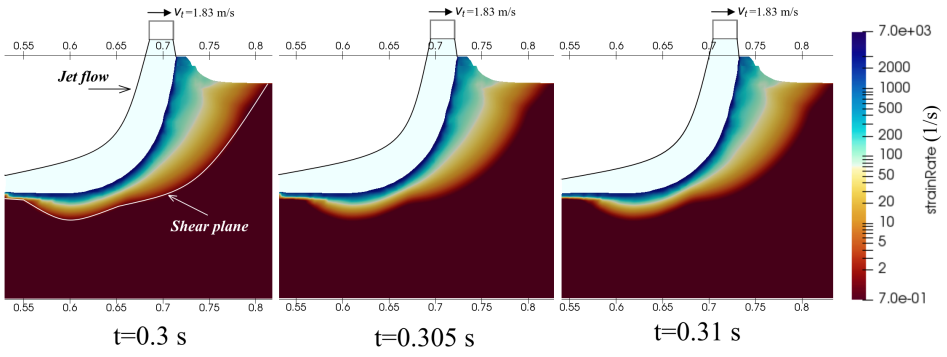

Figure 7.4: Shear plane patterns over time of deflecting jet. Jet traverse velocity is $v_t = 1.83\ m/s$. Jet ratio is $p_j/su = 19.5$. The shear rate is plotted on the soil. The shear plane pattern is marked by the white curve.

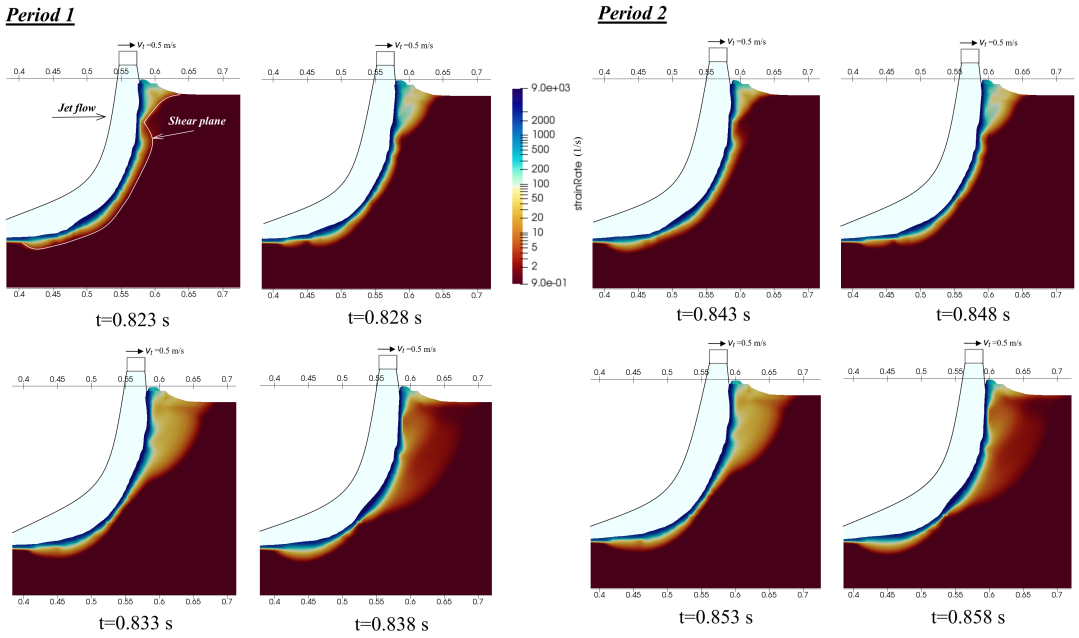

Figure 7.5: Shear plane patterns over time of penetrating jet. Jet traverse velocity is $v_t = 0.5\ m/s$. Jet ratio is $p_j/su = 38$. The strain rate is plotted on the soil. The shear plane is marked by the white curve. Two periods of shear plane change are shown. The period of the shear plane change is 0.02 s.

7.4 Jet inclination angle and deflection distance

To define when the jet starts deflecting, the inclination angle of the jet flow is used in this thesis. The inclination angle θ_j of the jet is calculated as:

$$\theta_j = atan(U_x/U_z) \tag{7.2}$$

where U_x and U_z are the x and z components of jet center line velocity U, see Fig.7.6. In this thesis, the threshold value of the inclination angle is set to be 5 degree. When the inclination angle θ_j is larger than 5 degree, the jet is determined to start deflecting.

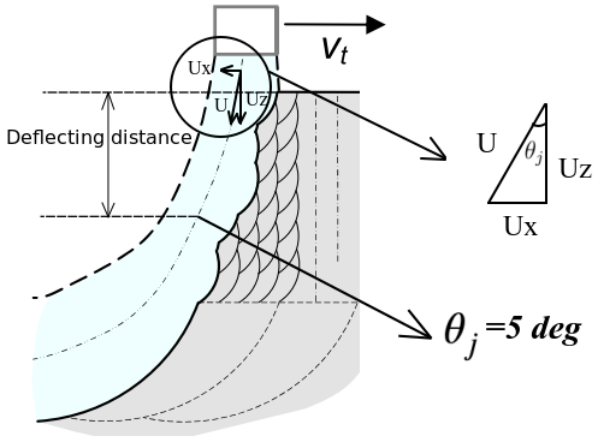

Figure 7.6: Definition of jet inclination angle and deflecting distance. U_x and U_z are the x and z components of jet center line velocity U. The deflecting distance is defined as the vertical distance between the soil surface and deflecting point. The deflecting point is the position where jet inclination angle is equal to 5 degree.

The depth where penetrating jet and deflecting jet start deflecting as a function of time is shown in Fig.7.7. This depth, which is called deflection distance in this thesis, is defined as the vertical distance from the soil surface to the deflecting point. The deflecting point is the position where jet inclination angle is equal to 5 degree.

It can be concluded from Fig.7.7 that the deflection distance of penetrating jet shows a periodic behavior. The changing period of the deflection distance for

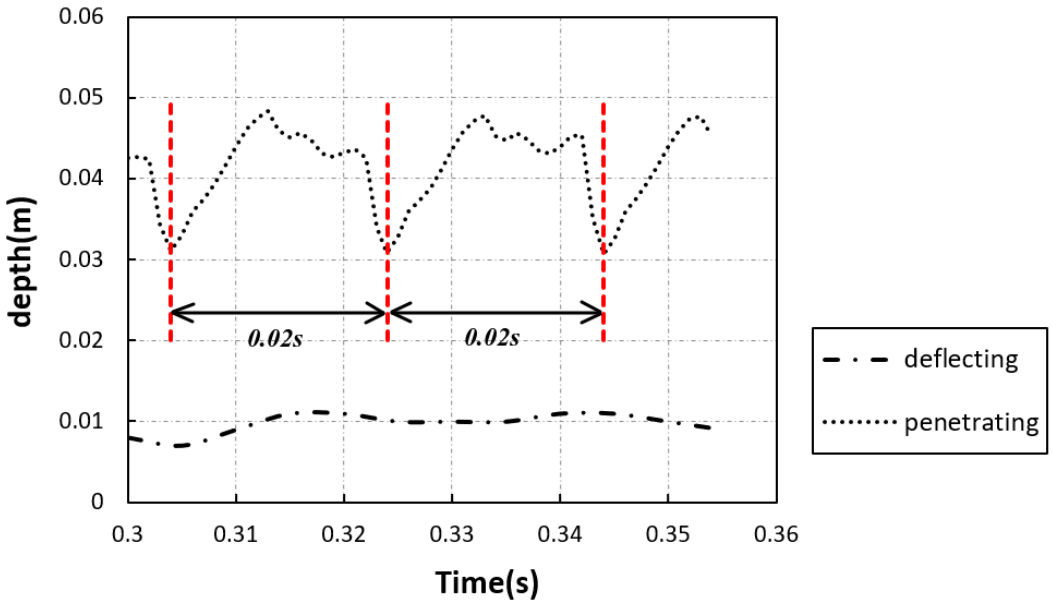

Figure 7.7: The deflection distance over time of penetrating jet and deflecting jet. The deflection distance is defined as the vertical distance between the soil surface and deflecting point. The deflecting point is the position where jet inclination angle is equal to 5 degree. The penetrating jet has a traverse velocity of 0.5 m/s and jet ratio 38. The deflecting jet has a traverse velocity of 1.83 m/s and jet ratio 19.5.

penetrating jet is 0.02 s, which is the same as the period of the shear plane change mentioned in section 7.3. The deflection distance of deflecting jet stays around 0.01 m, which does not change over time. This behavior also coincide the non-periodic behavior of the deflecting jet shear plane as shown in section 7.3.

It can also be concluded that the non-deflection zone of the penetrating jet does not have a constant depth. The depth of the non-deflecting zone is changing periodically. However, the deflection zone of the deflecting jet does not change during jetting process.

Chapter 8

Conclusions and recommendations

In this chapter, the conclusions and recommendations of this master thesis will be presented.

8.1 Conclusions

In this thesis, a CFD numerical model for simulating moving jet penetrating cohesive soil is built and validated with experimental work of Nobel (2013). Drift-flux model(Goeree et al., 2016) has been used modeling the sediment motion. Bingham plastic(Bingham, 1922) has been used modeling the cohesive soil. Dynamic mesh algorithms, AMI and A/R, are used modeling the moving jet. Besides, analysis based on this CFD model which was not recorded by the experiment is also conducted. The CFD model has the ability to reveal the details of the jetting process that could not be retrieved by the experiment.

8.1.1 Dynamic mesh model

In this thesis, two dynamic mesh algorithms, AMI and A/R, are found and used modeling the moving jet. AMI combined A/R dynamic mesh method is finally chosen for modeling the moving jet after a lock-exchange numerical validation. The combination of AMI and A/R dynamic mesh method is efficient, stable and accurate. By using this combination, a steady mesh region which separates the dynamic mesh region by AMI can exist during the simulation. The soil which is going to be jetted can be settled in this steady mesh region, increasing the simulation accuracy. The parallel calculation is also available for this combination, increasing the computational speed and saving computational time. The mesh quality stays constant during simulation, keeping the accuracy of the calculation. Besides, this combination allows for arbitrary geometry of the nozzle, which will be beneficial for optimizing the water injection dredging device.

8.1.2 Validation with experiment

Compared with experimental results from Nobel (2013), the following conclusions are found:

- Both deflecting jet and penetrating jet failure modes can be reproduced by the CFD model.
- Using the $buoyant - k - \epsilon$ turbulence model can relatively well predict the soil cavity depth compared with using the laminar model.
- A comparison of soil surface dislodgement rate between experiment and CFD simulation illustrates that the CFD simulation can have the same magnitude of soil production rate as the experiment.

8.1.3 Analysis based on CFD simulation

Besides the validation with experiment, analysis based on CFD simulation apart from the experiment are also carried out. From these analysis, the following conclusions are found:

- The soil volume dislodgement rate for a single moving jet increases as the jet traverse velocity increases when jet traverse velocity is lower than $1.83 m/s$.
- During jetting, the pressure will build up on the soil surface until the pressure is large enough to remove the soil.
- A shear plane determined by shear rate is defined. By observing the shear plane change over time, it can be found that the shear plane of the deflecting jet is not changing over time while the shear plane of penetrating jet is changing periodically.
- To determine when the jet starts deflecting, a jet inclination angle θ_j is defined. A threshold value of jet inclination angle, which is used to determine if the jet starts deflecting is set to be 5 degree in this thesis. When θ_j is over 5 degree, the jet is determined to start deflecting. The depth where the jet inclination angle is equal to 5 degree is called deflection distance in this study. The deflection distance of deflecting jet does not change over time. However, the deflection depth of penetrating jet is changing periodically.

8.2 Summary and Recommendations

This thesis work reveals that it is possible to describe the hydraulic excavation of cohesive soil with reasonable accuracy using CFD numerical model. The CFD model can also reveal details of the failure process that could not be retrieved from the experiments. Since the model is generic, the CFD approach can be applied for a jet bar with multiple nozzles. This can be helpful to improve the design of dredging equipment, optimize operational settings and estimate production. Based

on this thesis work, some recommendations for future research will be presented in this section.

- In this thesis work, the jetted material is the cohesive soil. Bingham plastic model has been implemented modeling the cohesive soil. In future study, the material can be replaced by non-cohesive materials (e.g. sand) or less cohesive materials (e.g. mud) to see the flexibility of this numerical model.
- As a limitation of both time and computational power, the mesh size is limited to a local size of 0.005 m. As a result, some physics behind cannot be revealed. If more computational power is available in the future, a calculation with finer mesh can be done to dig the physics.
- The optimization for the production of the soil is not done in this thesis. It is interesting to see how the production varies by changing the nozzle diameter, SOD (stand off distance) of the nozzle and even the water injection angle of the nozzle.
- Single moving jet cases have been carried out in this thesis. Multiple jets cases can be done in the future.

Appendix A

Derivation of drift-flux model

Definitions

Drift-flux model uses continuum theory to describe the motion of the sediments. Continuum theory deals with the mechanical behavior of materials modeled as a continuous mass rather than as discrete particles. Instead of describing the motion of single soil particles (e.g. silt, sand and clay particles), using continuum theory saves lots of computational power.

The average amount of volume occupied by a sediment fraction is defined as:

$$\alpha_k = \frac{V_k}{V_0} \tag{A.1}$$

where α_k is the volume concentration of phase k, V_k is the volume of phase k, V_0 is the total volume. V_0, the total volume also includes the carrier fluid phase is defined as $V_0 = \sum_{k=1}^{N} \alpha_k$. The total volume concentration as defined should follow:

$$\sum_{k=1}^{N} \alpha_k = 1 \tag{A.2}$$

where N is the total amount of phases. The mixture density is defined as:

$$\rho_m = \sum_{k=1}^{N} \rho_k \alpha_k \tag{A.3}$$

where ρ_k is the density of phase k. The mixture velocity is calculated by mass weighted averaged, the Favre averaging:

$$\mathbf{u_m} = \frac{1}{\rho_m} \sum_{k=1}^{N} \rho_k \alpha_k \mathbf{u_k} \tag{A.4}$$

where $\mathbf{u_m}$ is the mixture velocity, $\mathbf{u_k}$ is the velocity of phase k. The mass fraction c_k is given by:

$$c_k = \frac{\rho_k \alpha_k}{\sum_{k=1}^{N} \rho_k \alpha_k} = \frac{\rho_k \alpha_k}{\rho_m} \tag{A.5}$$

The relative velocity between the carrier fluid and phase k is defined as:

$$\mathbf{u_{kr}} = \mathbf{u_k} - \mathbf{u_f} \tag{A.6}$$

where $\mathbf{u_k}$ is the velocity of phase k, $\mathbf{u_f}$ is the velocity of the carrier fluid. When $k = 1$, $\mathbf{u_1} = \mathbf{u_f}$. The diffusion velocity, which is the relative velocity between mixture velocity and phase velocity is defined as:

$$\mathbf{u_{km}} = \mathbf{u_k} - \mathbf{u_m} \tag{A.7}$$

The diffusion velocity $\mathbf{u_{km}}$ also follows this relation:

$$\sum_{k=1}^{N} \alpha_k \rho_k \mathbf{u_{km}} = 0 \tag{A.8}$$

Mixture continuity equation

The mixture continuity equation for phase k is:

$$\frac{\partial \alpha_k \rho_k}{\partial t} + \nabla \cdot \alpha_k \rho_k \mathbf{u_k} = \Lambda_k \tag{A.9}$$

where Λ_k is the source term, denoting a phase transition. Due to sediment phase transitions are assumed to be absent, Λ_k is equal to zero. The continuity equation of phase k then reduces to:

$$\frac{\partial \alpha_k \rho_k}{\partial t} + \nabla \cdot \alpha_k \rho_k \mathbf{u_k} = 0 \tag{A.10}$$

Summing up continuity equation of all phases, it will obtain:

$$\frac{\partial}{\partial t}\sum_{k=1}^{N}\alpha_k\rho_k + \nabla\cdot\sum_{k=1}^{N}\alpha_k\rho_k\mathbf{u_k} = 0 \tag{A.11}$$

This is identical to:

$$\frac{\partial\rho_m}{\partial t} + \nabla\cdot(\rho_m\mathbf{u}_m) = 0 \tag{A.12}$$

Mixture momentum equation

For each sediment phase, the momentum equation is given by:

$$\begin{aligned}&\frac{\partial\alpha_k\rho_k\mathbf{u_k}}{\partial t} + \nabla\cdot(\alpha_k\rho_k\mathbf{u_k}\mathbf{u_k}) = \\ &-\nabla\alpha_k p_k + \nabla\cdot(\alpha_k\mathbf{T}_k + \alpha_k\mathbf{T}_k^t) + \alpha_k\rho_k\mathbf{g} + \alpha_k\mathbf{m}_k\end{aligned} \tag{A.13}$$

$\mathbf{T}_k$ and $\mathbf{T}_k^t$ are viscous and turbulent shear stress tensors respectively. $\mathbf{m}_k$ is the source term contributed by interacting force between each volume fraction. p_k is the pressure of phase k. $\mathbf{g}$ is the gravitational acceleration vector. Summing up momentum equation of all sediment phases:

$$\begin{aligned}&\frac{\partial}{\partial t}\sum_{k=1}^{N}\alpha_k\rho_k\mathbf{u_k} + \nabla\sum_{k=1}^{N}(\alpha_k\rho_k\mathbf{u_k}\mathbf{u_k}) = \\ &-\nabla\sum_{k=1}^{N}\alpha_k p_k + \nabla\cdot\sum_{k=1}^{N}(\alpha_k\mathbf{T}_k + \alpha_k\mathbf{T}_k^t) + \\ &\sum_{k=1}^{N}\alpha_k\rho_k\mathbf{g} + \sum_{k=1}^{N}\alpha_k\mathbf{m}_k\end{aligned} \tag{A.14}$$

Substitute Eq.(A.3), Eq.(A.4), Eq.(A.7) and Eq.(A.8) into Eq.(A.14), the momentum equation finally becomes:

$$\begin{aligned}&\frac{\partial\rho_m\mathbf{u}_m}{\partial t} + \nabla\cdot\rho_m\mathbf{u}_m\mathbf{u}_m = \\ &-\nabla p_m + \nabla\cdot(\mathbf{T}_m + \mathbf{T}_m^t - \sum_{k=1}^{N}\alpha_k\rho_k\mathbf{u}_{km}\mathbf{u}_{km}) + \rho_m\mathbf{g}\end{aligned} \tag{A.15}$$

where the internal force $\mathbf{m}_k$ is canceled out when summing up all phases. The $\mathbf{u}_{km}$, which is the diffusion velocity needs to be closed. The detail of closing this term refers to Richardson and Zaki (1954).

Phase transport equation

The closure of the concentration term α_k in the mixture momentum equations is accomplished by using phase transport equation:

$$\frac{\partial \alpha_k}{\partial t} + \nabla \cdot (\mathbf{u}_k \alpha_k) = 0 \tag{A.16}$$

Bibliography

Angioletti, M., Nino, E., and Ruocco, G. (2005). CFD turbulent modelling of jet impingement and its validation by particle image velocimetry and mass transfer measurements. *International Journal of Thermal Sciences*, 44(4):349–356.

Beaudoin, M. and Jasak, H. (2008). Development of a Generalized Grid Interface for Turbomachinery simulations with OpenFOAM. *Talk*, (December 2008):1–11.

Bingham, E. C. (1922). *Fluidity and plasticity*, volume 2. McGraw-Hill.

Cardiff, P., Tukovic, Z., Karac, A., and Ivankovic, A. (2014). Nonlinear solid mechanics in openfoam. In *9th OpenFOAM Workshop, University of Zagreb, Croatia*.

Craft, T. J., Graham, L. J. W., and Launder, B. E. (1993). Impinging jet studies for turbulence model assessment-ii. an examination of the performance of four turbulence models. *International Journal of Heat and Mass Transfer*, 36(10):2685–2697.

Demirdzic, I. and Peric, M. (1988). Space conservation law in finite volume calculations of fluid flow. *International Journal for Numerical Methods in Fluids*, 8(December 1987):1037–1050.

Drew, D. A. (1983). Mathematical modeling of two-phase flow. *Annual review of fluid mechanics*, 15(1):261–291.

Farrell, P. and Maddison, J. (2011). Conservative interpolation between volume meshes by local Galerkin projection. *Computer Methods in Applied Mechanics and Engineering*, 200(1-4):89–100.

Farrell, P., Piggott, M., Pain, C., Gorman, G., and Wilson, C. (2009). Conservative interpolation between unstructured meshes via supermesh construction. *Computer Methods in Applied Mechanics and Engineering*, 198(33-36):2632–2642.

Ferziger, J. H. and Peric, M. (2012). *Computational methods for fluid dynamics*. Springer Science & Business Media.

Gill, A. (2016). driftfluxdymfoam. `https://github.com/fruitynoodles/driftFluxDyMFoam`.

Goeree, J. C., Keetels, G. H., Munts, E. A., Bugdayci, H. H., and van Rhee, C. (2016). Concentration and velocity profiles of sediment-water mixtures using the drift flux model. *Canadian Journal of Chemical Engineering*, 94(6):1048–1058.

Greenshields, C. J. (2018). Openfoam user guide. *OpenFOAM Foundation Ltd, version*, 3(1):47.

Groen, E. C. (2016). Rotational jetting in clay.

Heyerichs, K. and Pollard, A. (1996). Heat transfer in separated and impinging turbulent flows. *International Journal of Heat and Mass Transfer*, 39(12):2385–2400.

Hiltunen, K., Jäsberg, A., Kallio, S., Karema, H., Kataja, M., Koponen, A., Manninen, M., and Taivassalo, V. (2009). Multiphase flow dynamics. *Theory and Numerics. Tech. Rep*, 722.

Holzinger, G. (2015). Openfoam–a little user-manual. *CD-Laboratory-Particulate Flow Modelling Johannes Keplper University, Linz, Austria*.

Ishii, M. and Hibiki, T. (2010). *Thermo-fluid dynamics of two-phase flow*. Springer Science & Business Media.

Jakobsen, H. A. (2014). *Chemical reactor modeling*. Springer.

Jaramillo, J. E., Pérez-Segarra, C. D., Rodriguez, I., and Oliva, A. (2008). Numerical study of plane and round impinging jets using RANS models. *Numerical Heat Transfer, Part B: Fundamentals*, 54(3):213–237.

Jaramillo, J. E., Trias, F. X., Gorobets, A., Pérez-Segarra, C. D., and Oliva, A. (2012). DNS and RANS modelling of a turbulent plane impinging jet. *International Journal of Heat and Mass Transfer*, 55(4):789–801.

Kubacki, S. and Dick, E. (2010). Simulation of plane impinging jets with k–ω based hybrid RANS/LES models. *International Journal of Heat and Fluid Flow*, 31(5):862–878.

Mangani, L., Buchmayr, M., and Darwish, M. (2014). Development of a novel fully coupled solver in OpenFOAM: Steady-state incompressible turbulent flows in rotational reference frames. *Numerical Heat Transfer, Part B: Fundamentals*, 66(6):526–543.

Manninen, M., Taivassalo, V., Kallio, S., et al. (1996). On the mixture model for multiphase flow.

Menon, S. and Schmidt, D. P. (2011). Conservative interpolation on unstructured polyhedral meshes: An extension of the supermesh approach to cell-centered finite-volume variables. *Computer Methods in Applied Mechanics and Engineering*, 200(41-44):2797–2804.

Nobel, A. J. (2013). *On the excavation process of a moving vertical jet in cohesive soil*. PhD thesis, Delft University of Technology.

Park, T. H., Choi, H. G., Yoo, J. Y., and Kim, S. J. (2003). Streamline upwind numerical simulation of two-dimensional confined impinging slot jets. *International Journal of Heat and Mass Transfer*, 46(2):251–262.

Piscaglia, F., Montorfano, a., and Onorati, a. (2014). A Moving Mesh Strategy to Perform Adaptive Large Eddy Simulation of IC Engines in OpenFOAM ®. *International Multidimensional Engine Modeling User's Group Meeting 2014*, (June).

Rahimi, M. and Soran, R. A. (2016). Slot jet impingement heat transfer for the cases of moving plate and moving nozzle. *Journal of the Brazilian Society of Mechanical Sciences and Engineering*, 38(8):2651–2659.

Rhie, C. and Chow, W. L. (1983). Numerical study of the turbulent flow past an airfoil with trailing edge separation. *AIAA journal*, 21(11):1525–1532.

Richardson, J. and Zaki, W. (1954). The sedimentation of a suspension of uniform spheres under conditions of viscous flow. *Chemical Engineering Science*, 3(2):65–73.

Seyedein, S., Hasan, M., and Mujumdar, A. (1994). Modelling of a single confined turbulent slot jet impingement using various turbulence models. *Applied Mathematical Modelling*, 18(10):526–537.

Shin, J. O., Dalziel, S. B., and Linden, P. F. (2004). Gravity currents produced by lock exchange. *Journal of Fluid Mechanics*, 521:1–34.

Tsuji, Y., Kawaguchi, T., and Tanaka, T. (1993). Discrete particle simulation of two-dimensional fluidized bed. *Powder technology*, 77(1):79–87.

Van Leer, B. (1974). Towards the ultimate conservative difference scheme. ii. monotonicity and conservation combined in a second-order scheme. *Journal of computational physics*, 14(4):361–370.

Wesseling, P. (2001). Elements of computational fluid dynamics. *Lecture Notes WI*, 4011.

Wilcox, D. C. et al. (1998). *Turbulence modeling for CFD*, volume 2. DCW industries La Canada, CA.

Zienkiewicz, O. C., Taylor, R. L., Taylor, R. L., and Taylor, R. L. (2000). *The finite element method: solid mechanics*, volume 2. Butterworth-heinemann.

Zuber, N. and Findlay, J. (1965). Average volumetric concentration in two-phase flow systems. *Journal of heat transfer*, 87(4):453–468.